01 Jan 2024

Polar Stacking of Dipole Parallel-Aligned Monolayers of Unsymmetrical 1,4-Diphenyl-1,3-Butadienes Creates Nonlinear Optical Materials: Insights from Experiments Guide Structure Assignments

Harmeet Bhoday

Justin Nulsen

Steven P. Kelley

Rainer Glaser
Missouri University of Science and Technology, glaserr@mst.edu

Polar Stacking of Dipole Parallel-Aligned Monolayers of Unsymmetrical 1,4-Diphenyl-1,3-butadienes Creates Nonlinear Optical Materials: Insights from Experiments Guide Structure Assignments

Harmeet Bhoday, Justin Nulsen, Steven P. Kelley, and Rainer Glaser*

Read Online

ACCESS | Metrics & More | Article Recommendations | Supporting Information

ABSTRACT: A series of 1-(4′-halophenyl)-4-(4″-methoxyphenyl)buta-1,3-dienes, (H, MeO, Y)-1,4-diphenylbuta-dienes with halogens Y = F (**1**), Cl (**2**), Br (**3**), and I (**4**) are described. Crystal structure analysis establishes that **1−4** present a new class of highly dipole parallel-aligned polar organic molecular materials for nonlinear optics (NLO). Building on previous studies of polar crystals of unsymmetrical acetophenone azines, (R, X, Y)-azines, X−Ph−CR═N−N═CR−Ph−Y (R = Me; X = R′O, PhO, R′OPh; Y = F, Cl, Br, I), we suspected that the all-carbon analogs (R, R′O, Y)-1,4-diphenylbutadienes, R′O−Ph−CR═CH−CH═CR−Ph−Y, could crystallize with polar lattices and feature stronger NLO effects because of their improved conjugation and higher

dipole moments. The key concept for the construction of polar crystals involves dipole parallel-aligned beloamphiphile monolayers (PBAMs) held together by double T-contacts. Butadienes engage in new types of (fe|fe) double T-contacts while PBAMs of azines employ (ef|fe) double T-contacts. Polar PBAM stacking results in perfect (**1**) or near-perfect (**2−4**) three-dimensional (3D) dipole parallel-alignment depending on the nature of the interlayer noncovalent interactions. The crystal architectures are discussed for **1−4**, and packing effects on chromophore conformations are assessed by comparison to potential energy surface analyses of the free molecules. The lower excitation energies of butadienes **1−4** are the primary origin of their higher hyperpolarizabilities relative to their azine analogs. Hyperpolarizabilities of **1−4** were computed for the free molecules in the gas phase and in solution phase (continuum models), measured in solution phase using the Lippert−Mataga equation (LME), and measured in the solid-state by powder second-harmonic generation (SHG). Overall, the results demonstrate that the series of (MeO, Y)-1,4-diphenylbutadienes presents a new class of polar crystalline materials with better performance parameters compared to the analogous (MeO, Y)-acetophenone azines. The results highlight that the optimization of a crystal property, such as the nonlinear optical (NLO) performance, must consider not only the desired molecular property but the design of the chromophore must be holistic with a view to the resulting supramolecular structure and account for the crucial role of interlayer interactions to control solid-state macroscopic properties.
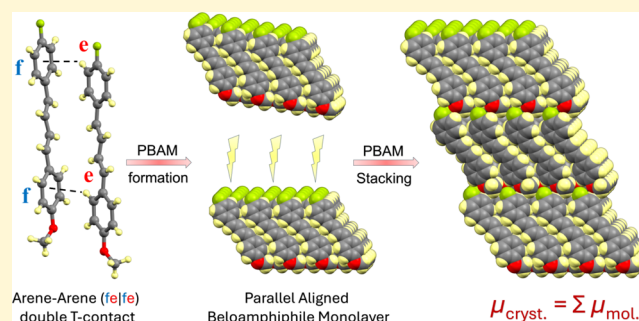
1. INTRODUCTION

Highly dipole parallel-aligned donor−acceptor substituted organic molecular crystals are appealing for their wide range of applications in the areas of nonlinear optics (NLO), optoelectronics, terahertz generation, electro-optics, photo-voltaics, and fluorescence.[1−8] For organic crystals to exhibit strong second-order NLO effects they must crystallize in a noncentrosymmetric space group. However, only a few crystals are known to adapt noncentrosymmetric space groups. For electrostatic reasons, the side-by-side molecular dipoles prefer an antiparallel arrangement while only the collinear dipoles would adopt parallel-alignment. This would predominantly generate nonpolar crystals that belong to centrosymmetric space groups. The achievement of large-scale polar order in

organic crystals was thought to be unattainable for a long time and continues to present a grand challenge. However, we have shown that the parallel-aligned dipole lattices may occur as local minima[9] with the implication that there is a chance to obtain polar crystals by rational design.

Our rational design strategy led to the fabrication of several series of donor−acceptor unsymmetrical acetophenone azines,

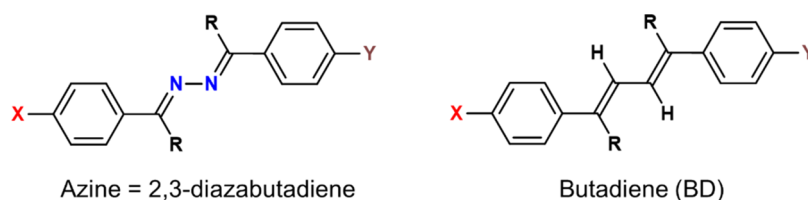**Scheme 1. Chemical Diagrams for the Unsymmetrical (R, X, Y)-Azines and Their Butadiene Analogs, (R, X, Y)-BD, Where X = R'O, and Y = Halogens**

Azine = 2,3-diazabutadiene   Butadiene (BD)

Scheme 2. General Synthesis for (MeO, Y)-Butadienes 1−4

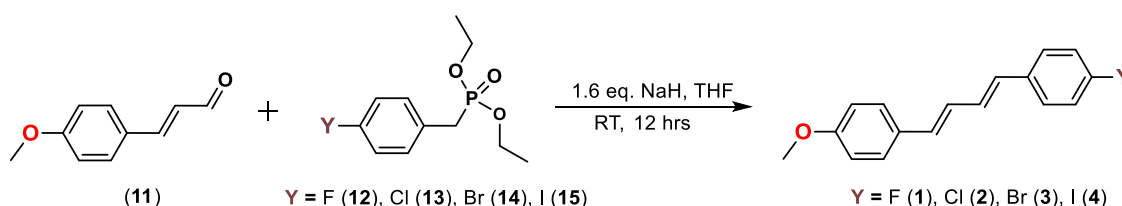(11)   Y = F (12), Cl (13), Br (14), I (15)   Y = F (1), Cl (2), Br (3), I (4)

Table 1. Experimental Crystallographic Parameters for (MeO, Y)-Butadienes

	1 (MeO, F) 2018	1 (MeO, F) 2023	2 (MeO, Cl) 2019	2 (MeO, Cl) 2023	3 (MeO, Br) 2022	4 (MeO, I) 2023
	disordered		disordered			
CCDC no.	1882215	2294067	1914558	2310885	2203168	2310884
crystal system	monoclinic	monoclinic	orthorhombic	orthorhombic	orthorhombic	orthorhombic
space group	$C2/c$	Cc	$Pbca$	$Pna2_1$	$Pca2_1$	$Pca2_1$
a/Å	28.4271(16)	28.4271(16)	7.2988(4)	6.1340(4)	6.1545(8)	6.2323(4)
b/Å	7.2368(4)	7.2368(4)	6.0350(3)	7.3297(6)	7.2555(10)	7.2311(5)
c/Å	6.3705(4)	6.3705(4)	31.3274(16)	30.894(2)	31.431(4)	31.659(2)
α/deg	90	90	90	90	90	90
β/deg	97.766(2)	97.766(2)	90	90	90	90
γ/deg	90	90	90	90	90	90
V/Å^3	1298.53(13)	1298.53(13)	1379.92(12)	1389.00(18)	1403.5(3)	1426.77(16)
Z/Z'	4/0.5	4/1	4/0.5	4/1	4/1	4/1
T/K	100	100	100	173	173	173
$R1$ $[I > 2\sigma(I)]$	0.0774	0.0440	0.1470	0.0414	0.0646	1.117
$wR2$ (all)	0.1941	0.1232	0.3393	0.1040	0.1537	0.0282
goodness-of-fit	1.210	1.047	1.151	1.140	1.183	0.0755

(R, X, Y)-azines, X−Ph−CR=N−N=CR−Ph−Y, where R = methyl, X = R'O, PhO, R'OPh, and Y = F, Cl, Br, I. Both perfect and near-perfect polar order was achieved with the azine systems. The first successful set was the methoxy-substituted unsymmetrical acetophenone azines, (Me, MeO, Y)-azines with Y = Cl, Br, I, where the parallel-aligned beloamphiphile layers (PBAMs) exhibit a near-perfect dipole parallel-alignment.[10−14] The next series was the decyloxy-substituted acetophenone azines, (Me, DecO, Y)-azines which led to three polar crystals with Y = F being perfectly parallel-aligned while Y = Cl, Br being near-perfect dipole parallel-aligned.[15−19] The PBAMs in the crystal structures of all these sets of azines are primarily stabilized by arene−arene double T-contacts. This further paved the way for phenoxy-substituted acetophenone azines, (Me, PhO, Y)-azines with one near-perfect (Y = F) and three perfect (Y = Cl, Br, I) dipole parallel-aligned crystals.[20−26] Biphenyl systems, (X, Y)-biphenyl without any spacer group also led to parallel-alignment in the crystals of (nBu, CN)-biphenyl,[27] (Me₂N, CN)-biphenyl,[28] (NO₂, I)-biphenyl,[29] and syn-(MeO, acetyl)-biphenyl.[30] This encouraged us to introduce a biphenyl moiety in the azine systems on one side to produce a brand new series of highly dipole parallel-aligned (Me, MeO-Ph, Y)-azines with three

near-perfect (Y = Cl, Br, I) and one perfect (Y = F) dipole parallel-aligned crystals.[31,32] We suspected that the butadiene analogs (R, X, Y)-butadiene as shown in Scheme 1 because of their large dipole moment larger conjugation lengths and higher dipole moments can produce stronger NLO effects than the azine systems if perfect dipole parallel-alignment can be achieved in their crystals.

Here we report on the synthesis of the methoxy series of (H, MeO, Y)-butadienes with the halogen substituents F (**1**), Cl (**2**), Br (**3**), and I (**4**).[33−36] For simplicity, we will refer to them as (MeO, Y)-butadiene throughout the text. We also considered the symmetrical (H, Y, Y)-butadienes with Y = F (**5**), Cl (**6**), Br (**7**), I (**8**), MeO (**9**), and H (**10**)[37,38] to compute asymmetrization energies. The general synthesis[39] for (MeO, Y)-butadienes **1−4** involves the Horner−Wadsworth−Emmons reaction of 4-methoxycinnamaldehyde (**11**) with diethyl(4-halobenzyl) phosphonate (**12−15**) as shown in Scheme 2.

The materials were characterized analytically by NMR spectroscopy (¹H, ¹³C, COSY, HSQC), vibrational spectroscopy (solid-state Fourier-transform infrared (FTIR)), and electron spectroscopy (UV/vis absorption, fluorescence). Single-crystals were grown and analyzed by single-crystal X-
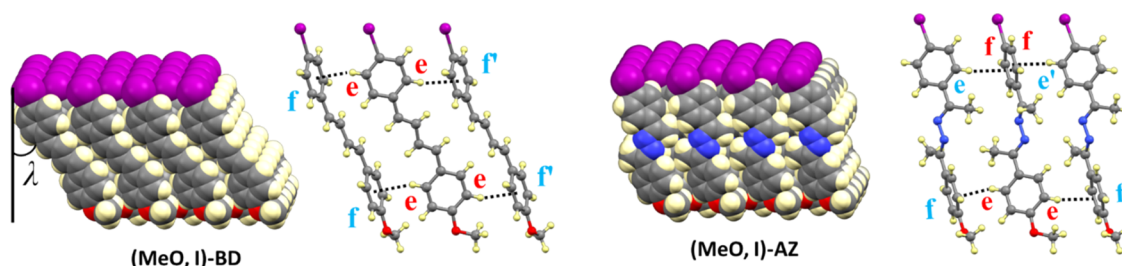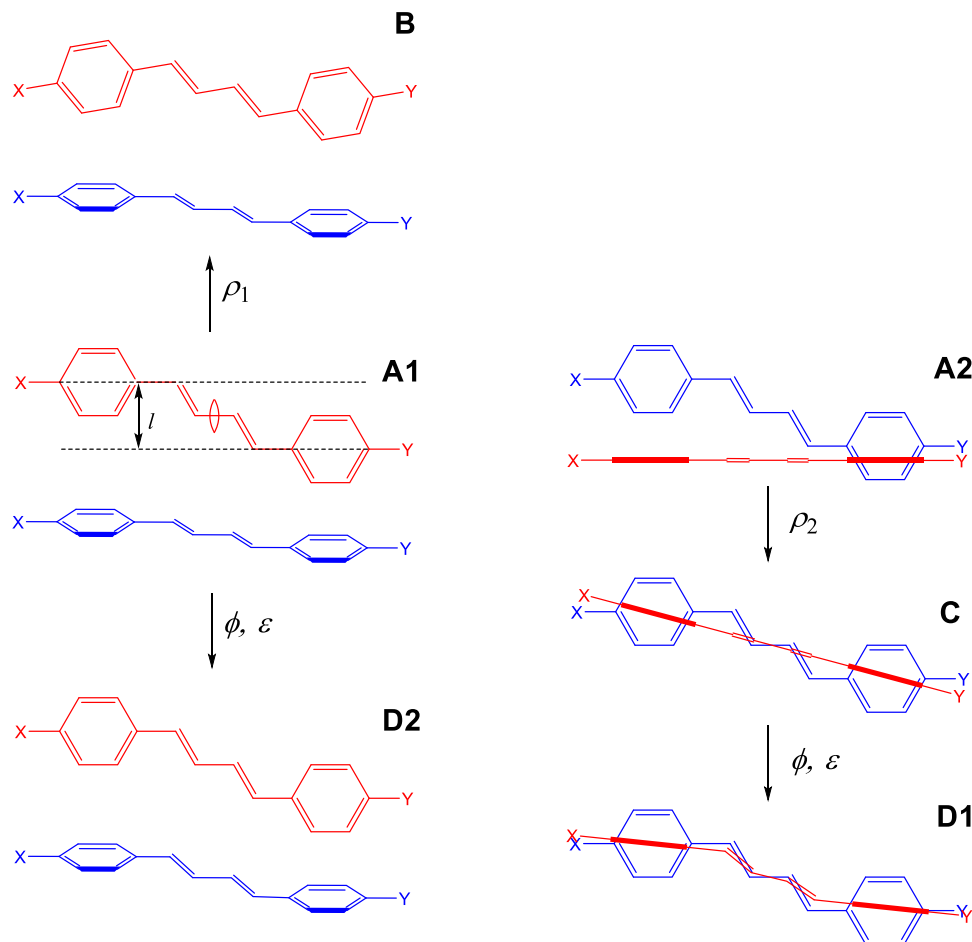
Figure 1. Molecular models of a parallel beloamphiphile monolayer (PBAM) in the crystal structure of (MeO, I)-BD (left) versus (MeO, I)-AZ (right).

Scheme 3. (fe|fe) Double T-Contact in Butadienes, the (f|f) Molecule in Blue and the (e|e) Molecule in Red[a]

[a]For simplicity, illustrations do not consider longitudinal offset and assume perpendicular approach.

ray crystallography. The butadienes crystallize with layered structures forming perfectly dipole parallel-aligned beloamphiphile monolayers (PBAMs), and that their polar stacking results in perfect 3D dipole parallel-alignment for **1** and near-perfect 3D dipole alignment for **2**−**4**. Their lattice architectures are described and compared to the azine analogs. Density functional calculations of asymmetrical butadienes **1**−**4** and symmetrical butadienes **5**−**10** were performed to study the conformational space of the butadienes and to determine asymmetrization energies. The dipole moments and hyperpolarizabilities of **1**−**4** are discussed relative to their azine analogs. Hyperpolarizabilities of **1**−**4** were computed for the free molecules in the gas phase and in solution phase (continuum models), measured in solution phase using the

Lippert−Mataga equation (LME), and measured in the solid-state by powder second-harmonic generation (SHG).

2. RESULTS AND DISCUSSION

2.1. Single Crystal Structure Determination. The results of the crystal structure analyses of the butadienes **1**−**4** are summarized in Table 1. The history of these crystal structure analyses provides an interesting case study of the interplay between single-crystal X-ray diffraction analyses and additional independent information about solid-state structures. The initial X-ray diffraction analyses suggested that the crystal structures of **1** and **2** were disordered whereas those of **3** and **4** were dipole parallel-aligned and all those results were submitted to CCDC with the submission numbers given in

Table 1. The quality of fit for all four crystal structure determinations was very good and there was no reason to doubt their validity. However, questions about the crystal structures of **1** and **2** arose upon receipt of the powder second-harmonic generation (SHG) data of the (MeO, Y)-butadienes with Y = F, Cl, Br. All three (MeO, Y)-BD proved to be SHG-active and the SHG intensities of **1** and **2** are found to be larger than that for the parallel-aligned **3**. These SHG data are incompatible with the disordered crystal structures with occupancies of 50% for both MeO and Y.

One could explain the SHG data with disordered structures of **1** and **2** if the occupations would be something different from 50:50. In the space groups $C2/c$ (**1**) and $Pbca$ (**2**), the crystallographic inversion centers force the two benzene rings to be identical and the occupancies must be fixed at 50%. Hence, we needed to refine the diffraction data in lower symmetry space groups, Cc for **1** and $Pna2_1$ for **2**.

The space group Cc was chosen manually for fluoro compound **1** as this is a subgroup of $C2/c$ in which all 2-fold symmetry has been removed, resulting in an asymmetric unit containing one entire molecule. Solution and refinement in this space group readily resulted in the fully ordered, dipole parallel-aligned 2023 structure. 94% of the molecule features essentially perfect inversion symmetry and only the super-position of O and F breaks this symmetry.

Since X-ray diffraction (XRD) is insensitive to small differences in atomic numbers between elements, this results in virtually no statistical indication that the structure is noncentrosymmetric. The normal crystallographic process never would have found the lower symmetry structure without supporting experiments. The highest symmetry space group that gives a reasonable refinement is considered the most reliable unless there are other experiments that suggest symmetry is forbidden. It is not particularly unusual for disorders like this to conceal the true structure.

We reexamined the structure of (MeO, Cl)-BD, **2** with a new data set. The solution of this data set resulted in the fully ordered refinement of the structure in $Pna2_1$ which was obtained in 2023 and submitted to CCDC. The lattice parameters differ from those of the disordered $Pbca$ structure we published earlier. The crystal measured in this latest XRD experiment probably is the true thermodynamic crystal structure of **2** considering its great similarity to the other unsymmetrical butadienes **3** and **4**. Typically, **2** formed thin, flaky films, and while these types of crystals also were present in the most recent sample, thick tabular crystals were used for the most recent measurement. The prior centrosymmetric model probably reflects polycrystallinity rather than disorder, but many other complicated forms of lattice defects could approximate disorder. Crystal growth conditions seemed to be very critical for the properties of this compound.

2.2. Crystal Packing of (MeO, Y)-Butadienes. The parallel-aligned beloamphiphile layers (PBAMs) in **1**−**4** exhibit perfect polar alignment. Figure 1 shows a molecular model of the (MeO, I)-butadiene PBAM and of one pair of neighboring molecules **4**. In the right-half of Figure 1 the analogous information is provided for the (MeO, I)-azine.

2.2.1. How to Account for Spacer Offset in (fe|fe) Double T-Contact. Each pair of butadienes interact via double T-contacts and the molecular model of the pair exemplifies the (fe|fe) double T-contact in the PBAMs where one butadiene interacts with two faces (f|f) and the other with two edges (e|

e). The molecules in the PBAM are mainly held together by arene−arene C−H⋯π intralayer interactions in the T-contacts.

In an ideal arene−arene T-contact, the orientations of the symmetry axes of the PhY units should be close to parallel and there may be some longitudinal offset (LonOS, n). The trans conformation of the butadiene spacer in 1,4-diphenylbuta-dienes causes a lateral offset (LatOS, l), which is defined by the distance between the local C_2-symmetry axes of the PhX and PhY arenes (Scheme 3). The illustrations **A1** and **A2** schematically show a pair of planar butadienes where the plane of the (ele) molecule is perpendicular to the plane of the (flf) molecule and the butadienes are arranged such that the PhY arenes can form a decent T-contact. It is obvious that the presence of significant lateral offset of $l \approx 1.86$ Å precludes the simultaneous formation of the T-contact between the PhX arenes. As a practical measure of the lateral offset l we determined the distances of the para-carbon of the anisole PhOMe from the lines defined by the ipso- and para-carbons of the haloarenes PhY and obtained the values $l(\mathbf{1}) = 1.92$ Å, $l(\mathbf{2}) = 1.88$ Å, $l(\mathbf{3}) = 1.82$ Å, and $l(\mathbf{4}) = 1.82$ Å.

One way to reduce the distance between the PhX moieties involves a rotation ρ_1 of the (ele) molecule around an axis through the C−C single bond of the spacer and perpendicular to the butadiene plane. This relative rotation **A1** → **B** naturally affects the distance between the faces and the two hydrogens on each edge: the meta-H of the PhY unit and the ortho-H of the PhX unit are placed closer to the arene faces. While rotation ρ_1 can bring the edge of the PhX unit closer to the plane of the (flf) molecule, the formation of a double T-contact requires a second type of rotation of the (ele) molecule **A2** → **C** by an angle ρ_2 about an axis through the C−C single bond of the spacer and coplanar with the butadiene plane. The approach of the (ele) molecule to the (flf) molecule by combination of rotations ρ_1 and ρ_2 causes the local C_2 axes of the PhX and PhY units to be noncollinear. A further optimization **C** → **D1** of the double T-contact can be achieved by (ϕ, ε) distortions of the spacer geometry which removes the coplanarity of the two arenes and instead places them in parallel planes. Of course, the (ϕ, ε) distortion also improves the distances between the two T-contacts, see **A1** → **D2**. We will discuss the (ϕ, ε) distortions and their relation to molecular helicity in more detail below.

The butadiene (felfe) double T-contact differs fundamentally from the double T-contacts in azines. The azines are characterized by the azine twist angle τ, and it is because of the azine twist that both azines engage one arene as a face and the other as an edge, either (elf) or (fle), and azine pair forms the azine double T-contact (eflfe).

2.2.2. Longitudinal Offset and PBAM Leaning Angle. The PBAM features a leaning angle λ, that is, the long axis of the butadiene is not perpendicular to the PBAM surface. The crystal structure shows $\lambda = 20.43°$ for the iodo butadiene **4** and this value may be compared to the value of $\lambda = 26.02°$ of the iodo azine analog.[20]

The (MeO, Y)-BD architectures for Y = F, Cl, Br, and I are completely analogous, and their leaning angles λ are 22.02° (F), 22.63° (Cl), 20.57° (Br), and 20.43° (I). The (Me, MeO, Y)-AZ architectures for Y = Cl, Br, I also are closely analogous, and their leaning angles λ are 25.65° (Cl), 25.83° (Br), and 26.02° (I). We have argued that the **A1** → **B** rotation ρ_1 of the (ele) molecule in combination with the **A2** → **C1** rotation ρ_2 places one hydrogen on each edge in closer proximity to the arene face (Scheme 3) and, importantly, the leaning angle λ
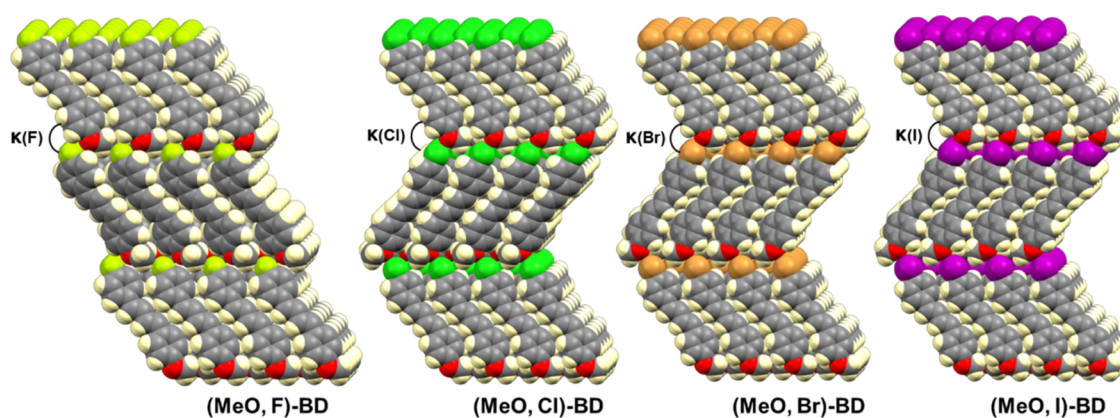
Figure 2. Space-filling bilayer presentations show disordered structures of (MeO, Y)-butadienes with Y = F and Cl (top) and near-perfect dipole parallel-alignment in crystals with Y = Br and I (bottom). The kink angles are $\kappa(F) = 0°$, $\kappa(Cl) = 137.74°$, $\kappa(Br) = 138.86°$, and $\kappa(I) = 139.14°$.

Table 2. Structural Parameters Describing the Methoxy Halogen Interactions[a]

Y	$d(Y\cdots O)$	$\angle(C_{Ph}-Y\cdots O)$	$\angle(C_{Ph}-O\cdots Y)$	$\angle(C_{Ph}-O\cdots Y\cdots C_{Me})$
F	3.15	100.6	105.2	140.8
Cl	3.09	167.3	126.7	145.3
Br	3.13	168.9	129.3	147.6
I	3.16	171.4	130.1	149.5
average[b]	3.13	169.2	128.7	147.5
std. dev.[b]	0.03	1.7	1.5	1.7

[a]Distances in Å and angles in degree. [b]Averages and standard deviations for the nonfluorine halogen species.

directly affects the geometry of the intralayer arene−arene interaction because this longitudinal offset places the proximate edge-H over the center of the arene-face. For the butadienes, it is the ortho-H of the fluoroarene H_o and the meta-H of the methoxyarene H_m of the (ele) butadiene that are placed over the faces of one neighboring (f|f) butadiene. This is illustrated in Figure 1 for (MeO, I)-BD **4** and the same is true for (MeO, Y)-BDs **1**−**3**. Of course, it is the meta-H of the fluoroarene H_m and the ortho-H of the methoxyarene H_o of the (ele) butadiene that are placed over the faces of the other neighboring (f'|f') butadiene.

We argue that the longitudinal offset is a direct consequence of the optimization of the T-contacts. An optimal T-contact in butadienes **1**-**4** places one edge-H over the centroid Σ (Greek S, Schwerpunkt, German = centroid) of the arene-face. This notion is supported by the structural parameters provided in Table S1 which lists for each T-contact in **1**−**4** the hydrogen distance above the arene face $h_{PhY} = d(\Sigma_{PhY}\cdots H)$ or $h_{PhOMe} = d(\Sigma_{PhOMe}\cdots H)$ and the associated angle $\nu_{PhY} = \angle(C_i\cdots\Sigma_{PhY}\cdots H)$ or $\nu_{PhOMe} = \angle(C_i\cdots\Sigma_{PhOMe}\cdots H)$. The angles ν_{PhY} and ν_{PhOMe} are defined with the ipso-C of the haloarene PhY or the anisole PhOMe, respectively, and describe the positioning of the hydrogen above the face centroid. Furthermore, we are providing the angles enclosed between the best planes of the interacting PhY or PhOMe moieties, $\angle(\Pi_{PhY}\cdots\Pi_{PhY})$ and $\angle(\Pi_{PhOMe}\cdots\Pi_{PhOMe})$.

The parameters for the nonfluorine systems **2**−**4** are very similar and Table S1 includes their averages and standard deviations. The hydrogens in **2**−**4** are placed 2.86 ± 0.04 Å above their faces and it is a stunning discovery that they are all placed right above the centroid with ν_{PhY} and ν_{PhOMe} angles well within 2° of 90°. We will show that the supramolecular architecture of **1** differs from those of **2**−**4** because of significant differences in the interlayer interactions. A first

indication of the unique crystal structure of **1** is provided by the larger deviation of ν_{PhF} and ν_{PhOMe} from orthogonality. The angles enclosed between the best planes of the arenes all are within 60 ± 3° and only the $\angle(\Pi_{PhY}\cdots\Pi_{PhY})$ angles for **3** and **4** are significantly reduced to about 53°.

We previously determined the crystal structures of the (Me, MeO, Y)-azines AZ-**2** (Y = Cl), AZ-**3** (Y = Br), and AZ-**4** (Y = I) and the PBAMs in their crystal structures also show characteristic leaning angles. The analysis for AZ-**2** and AZ-**3** is somewhat involved because these azines form kryptoracemic crystals, and in the present context we include only the data for iodoazine AZ-**4** in Table S1. The comparison of BD-**4** and AZ-**4** reveals surprisingly similar structures of the arene−arene double T-contacts, that is, in each T-contact one edge-H is placed over the centroid of the face arene and the edging arene encloses an angle of about 60° with the best plane of the face arene. In the case of the azines, it was reasonable to assume that the azine twist in combination with the phenyl twists would effect the arene−arene arrangement of the T-contacts. The new data on the butadienes suggest however that both classes of materials are capable of realizing essentially the same T-contact geometries.

2.2.3. Interlayer Interactions and PBAM Stacking Kink Angles. The polar stacking of PBAMs in the crystals of butadienes **1**−**4** as shown in Figure 2. Polar stacking involves positioning of the halogen surface of one PBAM close to the methoxy surface of the next PBAM. Perfect polar stacking is featured in fluorobutadiene **1** crystals: all molecules align their long axes identically in each layer. The other butadienes **2**−**4** display near-perfect polar stacking, where the molecular dipole directions in adjacent PBAMs alternate. The dipole moment perpendicular to the layer surface is oriented in the same direction across all layers while the smaller dipole component, the one parallel to the layer surface, is oriented in opposite

directions in adjacent PBAMs. The orientation of dipole directions in adjacent PBAMs is described by the kink angle κ, which is defined as the angle enclosed between the directions of the long axes of two molecules in the adjacent PBAMs. The kink angle for fluoro **1** is $\kappa(F) = 0°$ and Figure 2 shows kink angles of about $\kappa(Y) = 138.58 \pm 0.60°$ for **2–4**.

The halogen bonding between methoxy-O and the haloarenes is characterized by the $d(Y\cdots O)$ distances smaller than the vdW sum and $\angle(C_{Ph}-Y\cdots O)$ angles $\approx 180°$ (Table 2). From the perspective of the methoxy-arene, the halogen bonding would be most beneficial if the O-sp^2 lone-pair of the $C_{Ph}-O-C_{Me}$ moiety were coplanar with the halogen atom and pointed straight at it. In an ideal situation, one would expect an angle $\angle(C_{Ph}-O\cdots Y) \approx 120°$ and an improper dihedral $\angle(C_{Ph}-O\cdots Y\cdots C_{Me}) \approx 180°$. The interlayer architectures of **2–4** exhibit clear evidence of halogen bonding, their characteristic structural parameters fall in a narrow range, and the crystal structures optimize the position of the oxygen close to the $C_{Ph}-Y$ direction whereas it is less important that the halogen is placed in the phenyl methoxy plane.

In sharp contrast, halogen bonding does not play any role in the interlayer binding in fluoro **1**. Most remarkable is the deviation from the linearity quantified by $\angle(C_p-Y\cdots O) = 100.6°$. Instead, fluorobutadiene interacts with its interlayer neighbor via fluorine-methyl contacts, and their geometry is characterized by the distance $d(F\cdots H_{Me})$ and the angle $\angle(C-H_{Me}\cdots F)$, see Figure 3. Of the three methyl-Hs H_a, H_b and H_c only two engage in contacts with fluorine and $d(F\cdots H_c) = $ Å. The closer hydrogen H_a features a less ideal bonding angle ($d(F\cdots H_a) = 2.65$ Å, $\angle(C-H_a\cdots F) = 112.7°$) compared to H_b ($d(F\cdots H_b) = 2.87$ Å, $\angle(C-H_a\cdots F) = 96.7°$). In addition, the

methoxy-O binds one ortho-H of the fluoroarene with a short contact of $d(O\cdots H_o) = 2.65$ Å.

Our structural arguments about the interlayer interaction in **1–4** are fully corroborated by Hirshfeld surface analysis (Figure S1) and Hirshfeld two-dimensional (2D) fingerprint plots (Figure S2). Red spot on the Hirshfeld surfaces indicate the location of a prominent contact between atoms within vdW distance. Red spots manifesting the O⋯Y contacts appear on the Hirshfeld surfaces of **2–4**, but no such spots are present for fluoro compound **1**. Instead, the fluorobenzene moiety of **1** features two red spots in support of the F⋯H$_{Me}$ and O⋯H$_o$ contacts. These contacts are further corroborated by the spikes in the Hirshfeld 2D fingerprint plots.

2.3. Origin of the Butadiene Helicity in Crystals of 1–4. It is a characteristic feature of the butadienes in their solid-state structures **Xa** that they are not planar. Instead, they adopt helical structures in which the two arenes are placed in near-parallel planes. All crystal structures of **1–4** are true racemates.

To understand the origin of this characteristic distortion and its consequences, we analyzed their structures with the dihedral angles defined in Scheme 4 and their values are summarized in

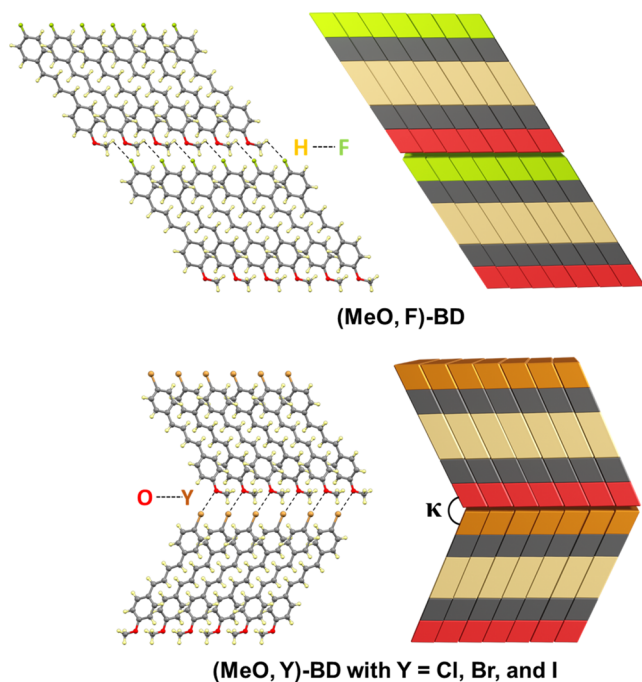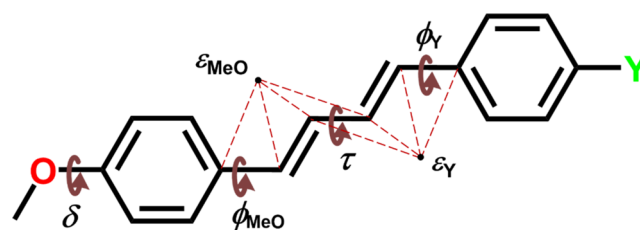**Scheme 4. Definition of Torsion Parameters about Single and Double Bonds**


Table 3. We computed the structures of the free butadienes at the APFD/6-311G(d) both for the two possible orientations of the MeO group, conformers **Xb** ($\delta = 180°$) and **Xc** ($\delta = 0°$). The isomer **Xb** shares the MeO orientation of **Xa** and there is a very small preference for **Xb** over **Xc**. Aside from the torsion angles about single bonds (τ, ϕ, δ), Table 3 includes the parameters ε_{MeO} and ε_Y to describe the nonplanarity of the alkene moieties. The results of the computations clearly show that the free butadienes are C_s-symmetric and hence, that the deviations from planarity in the crystals reflect packing effects.

The deviation from planarity renders the butadiene chiral and the consequences are exemplified for the crystal structure of (MeO, F)-BD **1** which is a true racemate. In Figure 4 are shown, the enantiomeric structures **1a** and **1a*** occurring in the crystal structure, and we need to define a parameter to distinguish these enantiomeric structures. Aside from the planar minima **1b** and **1c**, we optimized models **1d–1h** with the constraints specified in Figure 4 to understand the effects of alkene twists ε and phenyl twists ϕ on molecular geometry (Scheme 4) and we chose $|\varepsilon_{MeO}| = |\varepsilon_Y| = 165°$ for these models. Enantiomeric models **1d** and **1d*** show that ε_{MeO} and ε_Y values of opposite sign and equal magnitude lead to the placement of two arenes in parallel planes. It is important to recognize that the enantiomeric structures **1a** and **1a*** feature $|\varepsilon_{MeO}| \approx |\varepsilon_Y|$ and near parallel arene planes. We can use the sign of the difference $\Delta\varepsilon = \varepsilon_{MeO} - \varepsilon_Y$ to distinguish enantiomeric structures; for the models $\Delta\varepsilon$ (**1d**) $= -350°$ and $\Delta\varepsilon$ (**1d***) $= 350°$, for the crystal structure of the fluoro compound $\Delta\varepsilon$(**1a**) $= -351°$ and $\Delta\varepsilon$(**1a***) $= 351°$, and the data in Table 3 show

Figure 3. Perfect dipole parallel-aligned stacking of PBAMs in crystals of (MeO, F)-BD due to the directionality of interlayer weak F⋯H$_{Me}$ hydrogen bonding (top). Near-perfect dipole parallel-aligned stacking of PBAMs in crystals of (MeO, Y)-BD with Y = Cl, Br, and I due to the directionality of interlayer O⋯Y halogen bonding; note the zigzag pattern (bottom).

Table 3. Dihedral Angles of (MeO, Y)-Butadiene in Crystals and Gas Phase[a,b,c,d]

molecule		τ	ε_{MeO}	ε_Y	ϕ_{MeO}	ϕ_Y	δ	E_{rel}	$\Delta\varepsilon$
(MeO, F)	1a	180.6	175.7	−175.3	6.3	−6.1	175.7		351.0
	1b	180	180	180	0	0	180	0.000	
	1c	180	180	180	0	0	0	0.176	
(MeO, Cl)	2a	179.9	175.9	−175.2	5.6	−3.9	177.8		351.1
	2b	180	180	180	0	0	180	0.000	
	2c	180	180	180	0	0	0	0.179	
(MeO, Br)	3a	179.1	176.2	−175.0	5.5	−3.2	177.3		351.2
	3b	180	180	180	0	0	180	0.000	
	3c	180	180	180	0	0	0	0.180	
(MeO, I)	4a	179.7	175.6	−174.5	5.3	−2.4	−179.8		350.1
	4b	180	180	180	0	0	180	0.000	
	4c	180	180	180	0	0	0	0.180	

[a] $\tau = \angle(C_1{=}C_2{-}C_3{=}C_4)$, $\varepsilon_{MeO} = \angle(C_i{-}C_1{=}C_2{-}C_3)$, $\varepsilon_Y = \angle(C_i{-}C_4{=}C_3{-}C_2)$, ϕ_{MeO} and ϕ_Y employ the *syn* C_o atom, $\phi_{MeO} = \angle(C_o{-}C_i{-}C_1{=}C_2)$, $\phi_Y = \angle(C_o{-}C_i{-}C_4{=}C_3)$, δ employs the *syn* C_m atom, $\delta = \angle(C_m{-}C_i{-}O{-}C_{Me})$. [b] **Xa** describes the crystal structure, **Xb** and **Xc** are C_s-symmetric minima. [c] Energy E_{rel} in kcal/mol relative to most stable minimum. [d] All crystal structure data **Xa** refer to molecules with *P*-helicity. Note that the unique molecule in the crystal structures of **1**, **3**, and **4** are *P*-isomers while the unique molecule in the crystal structure of **2** happened to be the *M*-isomer.
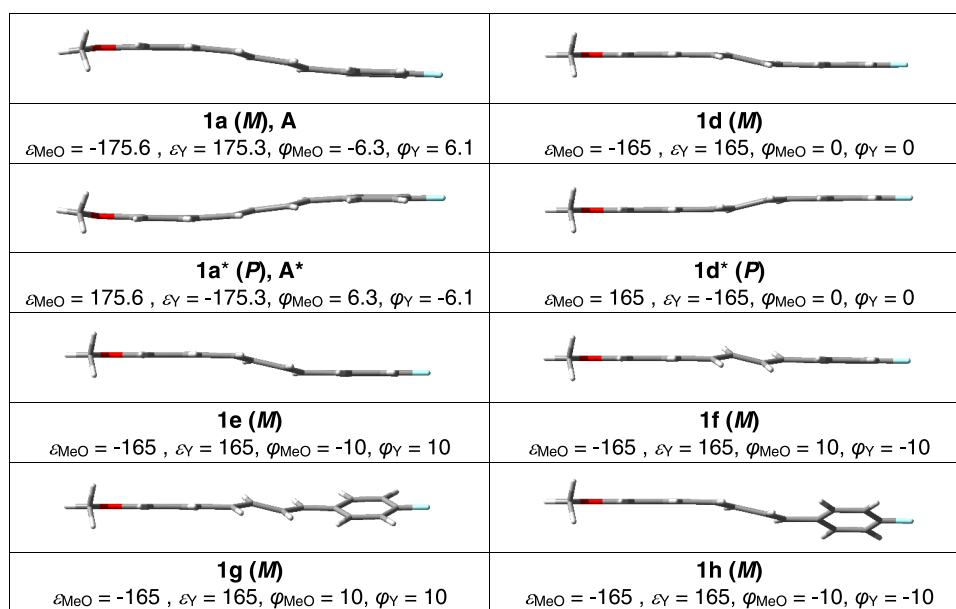
Figure 4. Interplay of single bond twists ϕ and alkene twists ε to define helicity and molecular shape of **1**.

that the $\Delta\varepsilon(\mathbf{Xa})$ and $\Delta\varepsilon(\mathbf{Xa*})$ values are very similar for all halogens. The chirality is the result of helical conformations and we refer to the enantiomeric structures with a negative or positive $\Delta\varepsilon$ value as the isomers with *M*- or *P*-helicity, respectively.

Models **1e−1h** show the effect of phenyl twisting and for simplicity of the models all phenyl twists are of equal magnitude (10°) and the focus is on the direction of these twists. Phenyl twists ϕ_{MeO} and ϕ_Y of opposite signs retain the two arenes in parallel planes and their signs may enhance (**1e**) or diminish (**1f**) the distance between these planes. Phenyl twists ϕ_{MeO} and ϕ_Y of equal sign (**1g** and **1h**) inevitably cause the two arenes to be in two nonparallel planes. The *M*-isomer of **1a** is similar to the *M*-isomer **1e**.

2.4. Computed Excitation Energies of (MeO, Y)-Butadienes and of (RO, Y)-Azines. The data in Table 4 show computed highest occupied molecular orbital−lowest-unoccupied molecular orbital (HOMO−LUMO) gaps (HLG) which are good approximations of the excitation energies based

on Janak's Theorem.[40] The data reveal that the E_{HLG} values follow the order 83.9 ± 0.8 kcal/mol for (H, MeO, Y)-BD < 92.6 ± 1.0 kcal/mol for (H, MeO, Y)-AZ < 99.0 ± 0.9 kcal/mol for (Me, MeO, Y)-AZ. The excitation energies are 99.5 ± 0.9 kcal/mol for (Me, PhO, Y)-AZ, and there is hardly any difference between the methoxy and phenoxy series of the acetophenones. Going from the flat butadienes to the equally flat benzaldehyde azines increases the excitation energy by 8.7 kcal/mol and twisting the spacer in the acetophenone azines raises the excitation energy by another 6.4 kcal/mol. The small standard deviations show that the nature of the Y substituent matters much less than the identity and the conformation of the −CH═E═ CH-spacer. The electronic absorption is mainly associated with the $\pi_2{\rightarrow}\pi_3$ excitation of the −CH═ E− E═CH− spacer. Molecular orbital theory easily explains the drastic reduction of the absorption energies of the butadienes (E═CH) compared to the respective azines (E═N), because the excitation is associated with E → CH electron density shifts.

Table 4. HOMO−LUMO Gap of Butadienes and Azines Computed at the APFD/6-311G* Level

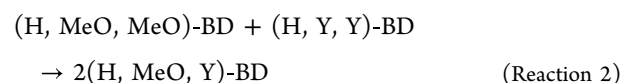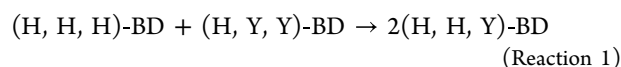| chromophore	ε_{HOMO} [au]	ε_{LUMO} [au]	λ_{HLG} [nm]	E_{HLG} [kcal/mol]
butadienes				
(H, MeO, F)-BD, **1**	−0.1983	−0.0626	336	85.2
(H, MeO, Cl)-BD, **2**	−0.2010	−0.0675	341	83.7
(H, MeO, Br)-BD, **3**	−0.2011	−0.0681	342	83.5
(H, MeO, I)-BD, **4**	−0.2017	−0.0693	344	83.0
(H, F, F)-BD, **5**	−0.2097	−0.0710	328	87.1
(H, Cl, Cl)-BD, **6**	−0.2151	−0.0799	337	84.8
(H, Br, Br)-BD, **7**	−0.2159	−0.0808	337	84.8
(H, I, I)-BD, **8**	−0.2159	−0.0829	343	83.4
(H, MeO, MeO)-BD, **9**	−0.1886	−0.0543	339	84.3
(H, H, H)-BD, **10**	−0.2068	−0.0676	327	87.4
azines				
(H, MeO, F)-AZ	−0.2202	−0.0701	304	94.2
(H, MeO, Cl)-AZ	−0.2223	−0.0750	309	92.5
(H, MeO, Br)-AZ	−0.2223	−0.0755	310	92.1
(H, MeO, I)-AZ	−0.2225	−0.0767	312	91.5
(Me, MeO, F)-AZ	−0.2177	−0.0576	285	100.5
(Me, MeO, Cl)-AZ	−0.2196	−0.0622	289	98.8
(Me, MeO, Br)-AZ	−0.2197	−0.0626	290	98.6
(Me, MeO, I)-AZ	−0.2201	−0.0637	291	98.1
(Me, PhO, F)-AZ	−0.2211	−0.0602	283	101.0
(Me, PhO, Cl)-AZ	−0.2227	−0.0644	288	99.4
(Me, PhO, Br)-AZ	−0.2228	−0.0648	288	99.1
(Me, PhO, I)-AZ	−0.2231	−0.0660	290	98.6
(H, H, H)-AZ	−0.2326	−0.0754	290	98.6
(Me, H, H)-AZ	−0.2306	−0.0588	265	107.8

We also computed the excitation energies for the symmetrical molecules (H, H, H)-BD, (H, H, H)-AZ, and (Me, H, H)-AZ, and they all are higher compared to the unsymmetrical systems. Asymmetrization has the smallest effect of about 3.5 kcal/mol on the butadienes, a larger effect of 6.1 kcal/mol on the flat azines, and by far the largest asymmetrization effect of about 8.8 kcal/mol for the twisted azines.

The energies computed for the symmetrical and unsymmetrical butadienes allow for the determination of the asymmetrization energies of the (H, Y)- and (MeO, Y)-butadienes according to Reactions 1 and 2, and the results for ΔE_{BD} and ΔG_{BD} are summarized in Table 5. Asymmetrization of butadiene always is associated with a negative asymmetrization energy for the formation of the (H, Y)- and (MeO, Y)-butadienes; as expected polarity increases bonding and donor−acceptor systems benefit the most.

Table 5. Asymmetrization Energies of (H, Y)- and (MeO, Y)-Butadienes[a]

(H, Y)	ASE-BD ΔE_{BD}	ASE-BD ΔG_{BD}	(MeO, Y)	ASE-BD ΔE_{BD}	ASE-BD ΔG_{BD}
(H, F)	−0.019	−0.092	(MeO, F)	−0.235	−0.124
(H, Cl)	−0.093	−0.211	(MeO, Cl)	−0.469	−0.417
(H, Br)	−0.105	−0.275	(MeO, Br)	−0.497	−0.443
(H, I)	−0.137	−0.297	(MeO, I)	−0.571	−0.506
(H, MeO)	−0.139	−0.246			

[a]Values in kcal/mol.

$$(H, H, H)\text{-BD} + (H, Y, Y)\text{-BD} \rightarrow 2(H, H, Y)\text{-BD}$$

(Reaction 1)

$$(H, MeO, MeO)\text{-BD} + (H, Y, Y)\text{-BD}$$
$$\rightarrow 2(H, MeO, Y)\text{-BD}$$

(Reaction 2)

2.5. Nonlinear Optical Performance Data of (MeO, Y)-Butadienes vs (MeO, Y)-Azines. *2.5.1. Computed First-Order Hyperpolarizabilities of the Free Molecule.* In Table 6,

Table 6. Computed Dipole Moments and Static First-Order Hyperpolarizabilities of (MeO, Y)-Butadienes and (MeO, Y)-Azines

molecule		μ_m[a]	β_o[b]	μ_m/V_{vdW}[c]	β_o/V_{vdW}[d]
(H, MeO, F)-BD	**1b**	3.3394	28.602	11.7136	100.327
	1c	3.1835	28.139	11.1669	98.704
(H, MeO, F)-AZ		3.3567	24.807	12.0535	89.080
(Me, MeO, F)-AZ		2.8952	15.269	7.3071	38.538
(Me, PhO, F)-AZ		2.7779	15.045	7.9878	43.261
(H, MeO, Cl)-BD	**2b**	4.1556	39.858	11.1724	107.160
	2c	3.9765	39.253	10.6909	105.532
(H, MeO, Cl)-AZ		4.0219	31.088	13.9831	108.083
(Me, MeO, Cl)-AZ		3.5252	18.441	8.8549	46.322
(Me, PhO, Cl)-AZ		3.3609	18.509	9.4166	51.859
(H, MeO, Br)-BD	**3b**	4.1495	40.155	11.8185	114.369
	3c	3.9623	39.528	11.2854	112.584
(H, MeO, Br)-AZ		3.9874	30.325	13.6696	103.959
(Me, MeO, Br)-AZ		3.4856	18.053	6.9896	36.202
(Me, PhO, Br)-AZ		3.3343	17.978	9.2367	49.803
(H, MeO, I)-BD	**4b**	4.3157	43.215	10.0098	100.232
	4c	4.1212	42.513	9.5585	98.605
(H, MeO, I)-AZ		4.0984	30.826	13.7672	103.549
(Me, MeO, I)-AZ		3.5960	19.166	9.5739	51.027
(Me, PhO, I)-AZ		3.4377	18.737	9.3676	51.058
PNA		7.2152	10.632	61.0919	90.022

[a]In Debye. [b]In ×10^{−30} esu. [c]In ×10^{−3} Debye Å^{−3}. [d]In ×10^{−33} esu Å^{−3}.

we report performance data computed at the APFD/6-311G* level. We determined molecular dipole moments and static first-order hyperpolarizabilities for the (H, MeO, Y)-butadienes and the equally flat (H, MeO, Y)-azines. For direct comparison, Table 6 includes the respective data recently reported for the methoxy and phenoxy series of acetophenone azines, the (Me, MeO, Y)-azines and (Me, PhO, Y)-azines, and the p-nitroaniline (PNA) standard.[20]

We have already shown that the methoxy **b**-conformation is energetically preferred and occurs in crystal structures. The data in Table 6 now show that $\mu_m(\mathbf{Xb}) > \mu_m(\mathbf{Xc})$ and $\beta_o(\mathbf{Xb}) > \beta_o(\mathbf{Xc})$ and hence the data for **Xb** are included in Figure 5.

The data points in Figure 5 are colored according to the four series of NLO compounds and each set is connected by straight lines to guide the eye. The properties of the chloro-, bromo-, and iodo-compounds are closely clustered while the fluoro-species are outliers in all cases with the lowest β_o and the lowest μ_m. The plot of β_o as a function of the E_{HLG} values listed in Table 4 demonstrates in a compelling fashion that the hyperpolarizabilities are inversely proportional to the electronic excitation energies and follow the order butadienes < flat benzaldehyde azines < twisted acetophenone azines. Note that even the fluorobutadiene features a higher β_o than any of the haloazines.
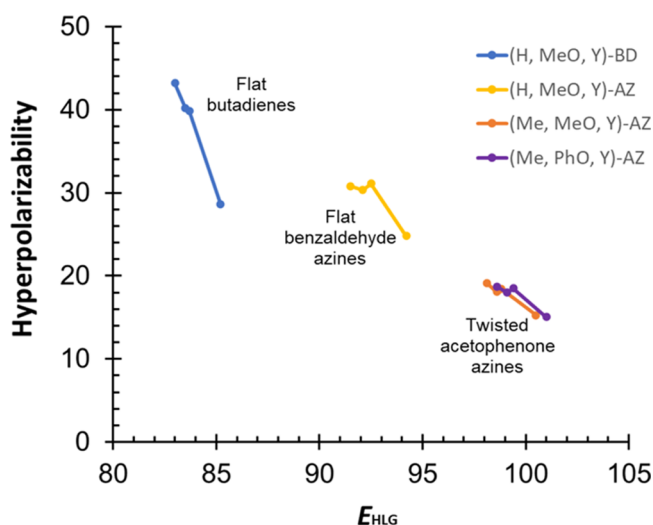
Figure 5. Static first-order hyperpolarizabilities β_o as a function of the excitation energies E_{HLG}. Computed data are shown with solid lines for (H, MeO, Y)-butadienes (blue), (H, MeO, Y)-azines (yellow), (Me, MeO, Y)-azines (orange), and (Me, PhO, Y)-azines (purple).

2.5.2. Computed First-Order Hyperpolarizabilities of (MeO, Y)-Butadienes 1−4 in Solvent Media. Computations of first-order hyperpolarizabilities β_0 are known to be affected by solvent effects,[41] and we computed β_0 values considering solvation using the SMD model[42] at the SMD(APFD/6-311G*)//APFD/6-311G* level. The results are listed in Table 7 and plotted as a function of the Δf solvent parameter in

Table 7. First-Order Hyperpolarizabilities β_0 and HOMO−LUMO Gap Energies E_{HLG} Computed for Different Solvent Media

molecule	gas-phase	benzene	chloroform	CH_2Cl_2	methanol
	First-Order Hyperpolarizabilities β_0 ($\times 10^{-30}$ esu)[a]				
1	28.602	51.140	67.345	75.930	82.739
2	39.858	73.502	97.467	110.879	121.728
3	40.155	75.493	98.255	114.769	124.020
4	43.215	73.649	94.312	105.604	113.174
	HOMO−LUMO Gap Energies E_{HLG} (kcal/mol)[a]				
1	85.2	85.1	85.1	85.2	85.3
2	83.7	83.6	83.6	83.6	83.8
3	83.5	83.3	83.4	83.2	83.4
4	83.0	83.0	83.1	83.1	83.3

[a]Computed at SMD(APFD/6-311G*)//APFD/6-311G* level.

Figure 6. The parameter Δf is characteristic for a solvent and defined by eq 1, where ε is the solvent's dielectric constant and n is its refractive index. The Supporting Information includes Table S2 to collect the solvent parameters ε, n, and Δf.

$$\Delta f = \frac{\varepsilon - 1}{2\varepsilon + 1} - \frac{n^2 - 1}{2n^2 + 1} \tag{1}$$

The mere presence of a continuum drastically increases the β_0 values. Even for the solvent benzene with its $\Delta f \approx 0$ the β_0 values are almost twice as large as the values computed for gas-phase ($\Delta f = 0$). Among the solvents examined we find a near linear dependence of β_0 with Δf. While the β_0 values follow the order 1 < 2 ≈ 3 < 4 in gas-phase, the order changes to 1 < 4 < 2 ≈ 3 in all polar solvents examined.

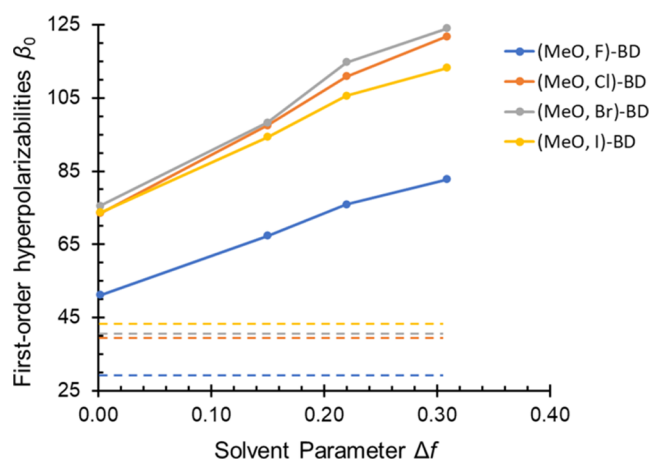**Figure 6.** Solvent dependence of computed first-order hyperpolarizabilities β_0 as a function of the solvent parameter Δf of (MeO, Y)-butadienes 1−4 and color codes for the identity of the halogen substituent. The gas-phase β_0 values serve as a reference and are included as horizontal dashed lines.

We have also computed the solvent effects on HOMO−LUMO gaps at the SMD(APFD/6-311G*)//APFD/6-311G* level (Table 7). The HOMO−LUMO gaps tend to modestly increase as a function of Δf or ε, and hence we assign the increase of β_0 with solvent polarity to a greater change in dipole moment upon excitation. We examined this relation experimentally as well (vide infra).

2.5.3. Measured First-Order Hyperpolarizabilities in Solution. 2.5.3.1. Hyperpolarizabilities via the Lippert−Mataga Equation. The frequency-independent component of the first-order hyperpolarizability β_0 can be determined experimentally via eq 2,[43] where $\Delta\mu_{ex}$ is the change in dipole moment in atomic units, M_{ge} is the transition dipole moment in atomic units, and $\hbar\omega_{ge}$ is the transition energy in atomic units.

$$\beta_0 = \frac{3(M_{ge})^2 \Delta\mu_{ex}}{2(\hbar\omega_{ex})^2} \tag{2}$$

$$hc(\Delta\nu_{ex}) = hc(\nu_{abs} - \nu_{em}) = \frac{2\Delta f \Delta\mu_{ex}^2}{4\pi\varepsilon_0 a^3} + C \tag{3}$$

$$\Delta\mu_{ex}^2 = S \cdot 2\pi\varepsilon_0 a^3 = \left(hc \cdot \frac{\Delta(\Delta\nu_{ex})}{\Delta(\Delta f)} \right) \cdot 2\pi\varepsilon_0 a^3 \tag{4}$$

The value $\Delta\mu_{ex}$ for each butadiene was determined via the Lippert−Mataga Equation eq 3, which relates $\Delta\mu_{ex}$ to the Stokes shift $\Delta\nu_{ex} = \nu_{abs} - \nu_{em}$, which is the difference between the wavenumbers (in cm^{-1}) of the maxima of absorption and fluorescence emission. The measurement of $\Delta\nu_{ex}$ for several solvents as a function of Δf allows one to eliminate the constant C and to evaluate $\Delta\mu_{ex}$ based on the determination of the slope $S = hc \cdot \frac{\Delta(\Delta\nu_{ex})}{\Delta(\Delta f)}$ of eq 4. In eqs 3 and 4, ε_0 is the vacuum permittivity ($4\pi\varepsilon_0 = 1.112 \times 10^{-10}$ C^2/N^{2}m^2), h is Planck's constant (6.626×10^{-34} Js), c is the velocity of light (2.99×10^8 m/s), and a is the Onsager radius (in meter). The Onsager radii of 1-4 were determined at the APFD/6-31G* level.

2.5.3.2. Absorption and Fluorescence Spectra of 1−4. The solvent dependency of $\Delta\nu_{ex}$ of 1−4 was evaluated for the
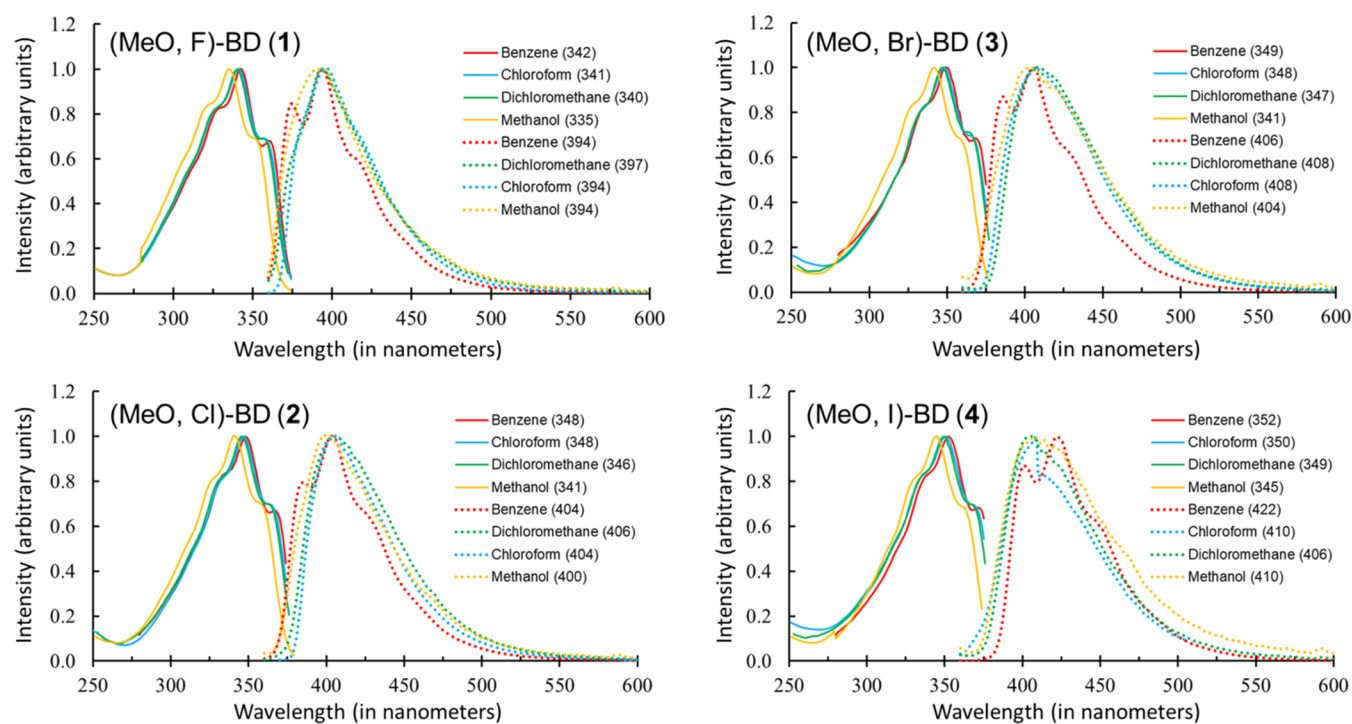
Figure 7. Normalized absorption and fluorescence spectra of (MeO, Y)-butadienes **1−4** (top to bottom). Solid lines for absorption spectra and short and long dashed lines for emission spectra. Solvent is indicated by line color benzene (red), chloroform (blue), dichloromethane (green), and methanol (yellow).

Table 8. First-Order Hyperpolarizabilities β_0 Measured by Evaluation of the Lippert−Mataga Equation

mol. (M)	Onsager radius, a (Å)	$S \pm S_{SE}$ (J)	$\Delta\mu_{ex}$ (au)	M_{ge} (au)	$\hbar\omega_{ge}$ (au)
1	0.532	3.4678 ± 1.3605	6.3585	4.3734	0.1357
2	0.527	3.4691 ± 1.3361	6.2703	4.5598	0.1334
3	0.546	4.5776 ± 1.3625	7.5958	4.6279	0.1331
4	0.602	4.0783	8.3004	4.7396	0.1323
	$\beta_{0,LL}$ ($\times10^{-30}$ esu)	$\beta_0 \pm \beta_{0,SE}$ ($\times10^{-30}$ esu)	$\beta_{0,UL}$ ($\times10^{-30}$ esu)	$\beta_0($ (M)$/\beta_0($**1**$)$ LME	DFT
1	66.71	85.578 ± 18.866	100.98	1.00	1.00
2	74.41	94.898 ± 20.486	111.69	1.11	1.39
3	99.83	119.116 ± 19.288	135.69	1.39	1.40
4	117.13	138.133 ± 21.000	155.13	1.61	1.51

solvents benzene, chloroform, dichloromethane (DCM), and methanol. We measured the absorption UV/vis spectra of (MeO, Y)-butadienes **1−4** in the four solvents benzene, chloroform, dichloromethane (DCM), and methanol, and we also measured the fluorescence spectra obtained after excitation at the wavelength of maximum absorption. The normalized absorption and fluorescence spectra are shown in Figure 7 and pertinent data (λ_{abs}, λ_{em}) are collected in Table S3. The Supporting Information also includes Figure S3 displaying plots of $\Delta\nu_{ex}$ as a function of Δf for **1−4** together with linear regression equations and standard errors computed by the LINEST method. These equations deliver the solvent dependent slopes S listed in Table 8 and allow for the determination of the solvent independent $\Delta\mu_{ex}$ values listed in Table 8 in atomic units.

2.5.3.3. Evaluation of the Lippert−Mataga Equation. We determined the transition energy $\hbar\omega_{ge}$ via the HOMO−LUMO gap (Table 4), and these values are listed as transition energies in atomic units in Table 8. The transition dipole moments M_{ge} were determined with time-dependent density

functional theory (TDDFT) at the APFD/6-311G* level and based on the ground state structures optimized at that same level; TD-APFD/6-311G*//APFD/6-311G*.

In Figure 8 are plotted the UV/vis absorption energies of **1−4** against the HOMO−LUMO gaps computed at the SMD(APFD/6-311G*)//APFD/6-311G* level (Table 7). The data measured for the different solvents are connected by straight lines and the line color codes for the solvents as in Figure 7. In a perfect world these plots would be straight lines with slope of unity and pointing at the coordinate origin, and we included the diagonal in gray as the pertinent reference. For methanol, the data very much meet expectations while the curves for the other solvents all are essentially parallel with the diagonal but with an offset that indicates an overestimation of the computed E_{HLG} values. The four data points in every line correspond to compounds **1−4** in that order. Deviations from linearity reflect the limitations of the continuum model to fully account for specific interactions with the solvent, and it appears that the chloro compound **2** causes the most deviation.
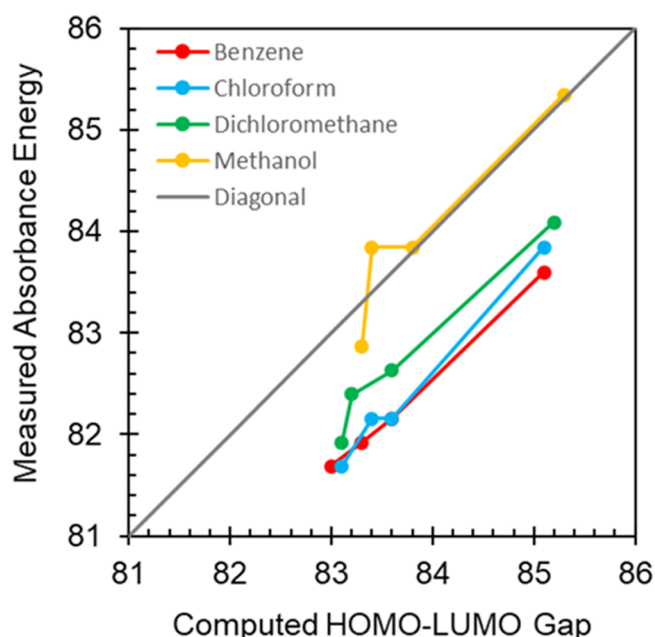
Figure 8. Plots of UV/vis absorbance energies (kcal/mol) as a function of computed HOMO−LUMO gaps (kcal/mol) for **1**−**4** in four solvents. Solvent is indicated by line color as in Figure 7.

Figure 9. First-order hyperpolarizabilities β_0 determined via the Lippert−Mataga equation for **1**−**4**. Error bars are determined via $\beta_{0,\text{LL}}$ and $\beta_{0,\text{UL}}$ based on the standard error S_{SE} of the solvent-dependent slopes of eq 4. Comparison data connected by dashed lines are discussed in the text.

Despite these caveats, Figure 8 shows remarkably good agreement between the spectroscopic data and theory.

The plots of $\Delta\nu_{\text{ex}}$ as a function of Δf (Figure S3) are not perfectly smooth and the consideration of standard error becomes imperative for the slope S. The uncertainties by the LINEST method are included in Table 8 for **1**−**3**. The fluorescence spectrum of iodo compound **4** features high Stokes shifts and **4** apparently enjoys an iodo-specific stabilization of its excited state. Using slopes S and their standard errors S_{SE}, we computed three β_0 values: $\beta_{0,\text{LL}}$, β_0, and $\beta_{0,\text{UL}}$. The β_0 values are derived directly using the S values themselves and the lower limit $\beta_{0,\text{LL}}$ and upper limit $\beta_{0,\text{UL}}$ values were determined using the $S - S_{\text{SE}}$ and $S + S_{\text{SE}}$ values, respectively. The standard errors listed for β_0 are the greater of the differences between β_0 and $\beta_{0,\text{LL}}$ or $\beta_{0,\text{UL}}$. For iodo compound **4**, $\beta_{0,\text{SE}}$ is an estimate based on data for **1**−**3**. Figure 9 shows the measured β_0 values along with their estimated errors. For comparison, we included in Figure 9 the computed gas-phase β_0 values in Table 6 (black dashed line) and the computed solution-phase β_0 values in Table 7 (dot-dashed lines color code for solvents as in Figures 7 and 8).

Figure 9 shows that the butadienes **1**−**4** are substantially more hyperpolarizable than azines, that their hyperpolarizabilities in condensed-phase greatly exceed the gas-phase values, that the measured β_0 values follow the order **1** < **2** < **3** < **4**, and that the ratios $\beta_0(\text{M})/\beta_0(\textbf{1})$ determined with the LME derived values (Table 8) show substantial increases in that sequence. The gas-phase computations predict fluorine to be the outlier with the chlorine, bromine, and iodine compounds closely grouped together and, moreover, the DFT derived ratios $\beta_0(\text{M})/\beta_0(\textbf{1})$ suggest a small advantage for iodine. The SMD continuum solvation model correctly reflects the general increase of the hyperpolarizabilities in condensed-phase, but the model consistently underestimates solvation effects of benzene. For the nonaromatic solvents, the SMD computed data for **1**−**3** fall within the error bars of the measurements. However, the SMD data do not reflect the
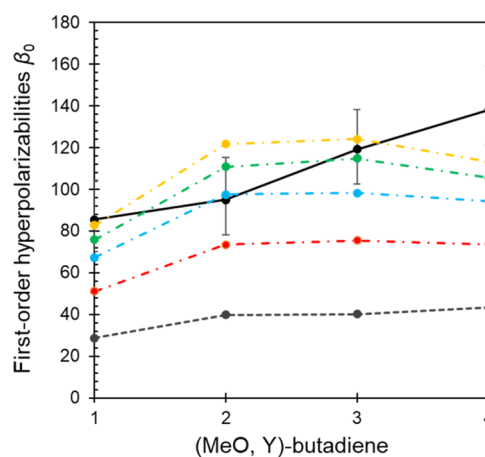
higher hyperpolarizability of bromo-**3** compared to chloro-**2** and the data for iodo-**4** are underestimated substantially.

2.5.4. Powder Second-Harmonic Generation Data of (MeO, Y)-BD. Second harmonic generation data were measured in the Halasyamani laboratory using a modified Kurtz-Perry powder laser system[44] with reference to a KDP (potassium dihydrogen phosphate) standard and phase-matching tests were not performed.[45] Centrosymmetric crystals of PNA also were measured as a negative control. A Nd:YAG laser (1064 nm) was employed and the SHG was measured at 532 nm (green). The powder samples (ca. 50 mg) were placed in fused silica tubes. The powders of the crystalline organic molecular materials featured small particle sizes and the most appropriate particle size was selected for the KDP reference (75−90 μm).

Oscilloscope traces of the measurement of the (MeO, Y)-butadienes with Y = F, Cl, and Br are shown in Figure 10 and allow for several important conclusions. Most importantly, the powder SHG measurements provide clear evidence that the powders of the butadiene materials are SHG active. It was this
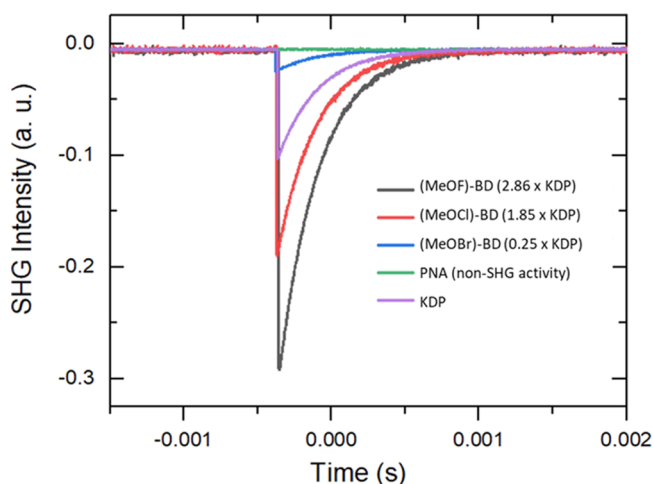

Figure 10. Measured powder SHG signals of (MeO, Y)-butadiene samples and KDP standard at 1064 nm.

information that led to the reexamination of the crystal structures of butadienes **1** and **2** (vide supra).

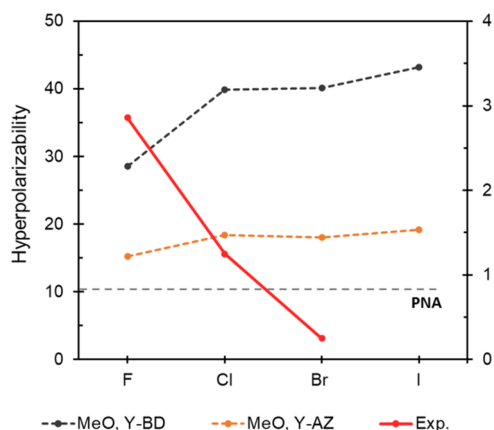Figure 11 provides for a comparison of the computed molecular hyperpolarizabilities β_o (primary axis) and the

Figure 11. Halogen dependence of the computed first-order hyperpolarizabilities β_o of (MeO, Y)-azines (orange dashed) and (MeO, Y)-butadienes (black dashed) using the primary axis in units of 10^{-30} esu. Solid-state measured data are shown for the (MeO, Y)-butadienes (green) in units of KDP SHG intensity using the secondary axis.

powder SHG data (secondary axis). The SHG intensities follow the order **1** ($2.86 \times KDP$) > **2** ($1.85 \times KDP$) > **3** ($0.25 \times KDP$). One needs to be careful about the interpretation of powder SHG data because they depend on particle size and laser excitation wavelength. Even with such caveats, the large difference between the measured SHG activities of **2** and **3** is unexpected because the chloro and bromo compounds have very similar crystal structures and the solution-phase measurements indicate the reverse order of their β_o values. The powder SHG data show the highest intensity for fluorobutadiene **1** even though the computations suggest that the molecular NLO response of the fluoro-**1** is the lowest in the series. It is this feature that brings to the fore the importance of the mode of PBAM stacking and the comparative discussion of **1** and **2** makes the point.

The stacking of PBAMs matters greatly for the NLO performance of the crystal. Crystal structures with perfect PBAM stacking ($\kappa = 0$) are expected to show maximal NLO performance because the dipole moments of molecules in all layers are parallel-aligned. On the other hand, crystal structures with near-perfect PBAM stacking suffer from some dipole moment cancelation between successive PBAMs and the effective dipole moment μ_{eff} equals the dipole moment perpendicular to the PBAM surface. Figure 12 illustrates the relative orientations of the molecules in two stacked PBAMs for the case of **1** ($\kappa = 0°$) and **2** ($\kappa = 137.7°$). The case of **2** is also representative of **3** and **4** and pertinent data for **1**-**4** are summarized in Table 9. We determined the angles Δ_{la} and Δ_{perp} enclosed between the computed molecular dipole moment μ_m (blue vector) and the long axis of the molecules (C2–C3 directions) or the dipole moment component μ_{perp} normal to the PBAM surface (red vector), respectively. For perfectly stacked PBAMs all dipole moments are aligned and the effective dipole moment μ_{eff} is approximately equal to the molecular dipole moment μ_m. For structures with kink angles the dipole moment perpendicular to the PBAM surface μ_{perp} is
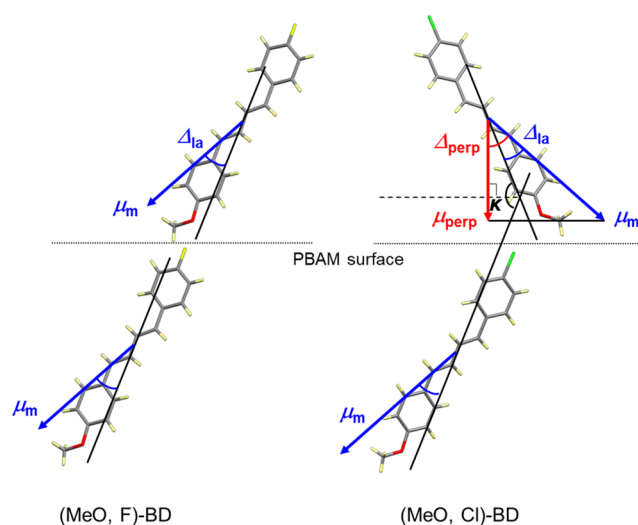

Figure 12. Relative dipole directions in stacked PBAMs of (MeO, F)-BD (left) and (MeO, Cl)-BD (right). PBAM surfaces are horizontal (dotted lines) and the kink angle κ describes the angle enclosed between long axes of molecules (solid black line) in the stacked PBAMs.

Table 9. Molecular Dipole Direction and Effective Dipole Moment[a,b]

	Δ_{la}	κ	Δ_{perp}	μ_m	μ_{eff}	μ_{eff}/μ_m
1	31.6	0.0		3.3394	3.3394	1.00
2	27.7	137.7	48.9	4.1556	2.7343	0.66
3	27.9	138.9	48.5	4.1495	2.7488	0.66
4	27.4	139.1	47.9	4.3157	2.8957	0.67

[a]See Figure 12 for definitions, angles in degrees, dipole moments in Debye. [b]$\Delta_{perp} = \Delta_{la} + \lambda$ for **1**, and $\Delta_{perp} = \Delta_{la} + \lambda = \Delta_{la} + 90 - 0.5\kappa$ for **2**−**4**.

the effective dipole moment and μ_{perp} can be computed via $\Delta_{perp} = \Delta_{la} + 90 - 0.5\kappa$ and $\mu_{eff}/\mu_m = \cos(\Delta_{perp})$.

The materials **2**−**4** feature interlayer halogen bonding and therefore result in PBAM stacking with kink angles κ of about equal magnitude. Consequently their Δ_{perp} values also are essentially the same and only two-thirds of their molecular dipole moments contribute to their crystal dipole moments ($\mu_{eff}/\mu_m = 0.66$). It is the perfect stacking of the PBAMs of the fluoro compound $\kappa = 0$ that provides an advantage of about 22% for the effective dipole moment μ_{eff} of crystals of **1** compared to **2**−**4**. Note that this increase of the crystal dipole is realized for **1** even though the molecular dipole of **1** is about 20% lower compared to **2**−**4**.

3. EXPERIMENTAL SECTION

3.1. Butadiene Syntheses and Analytical Characterization. *3.1.1. Materials and General Methods.* Reagents and solvents used in all experiments were sourced from Arcos Organics, TCI, and Alfa Aesar—distributed by Fischer Scientific and Millipore Sigma—and/ or otherwise provided by the Missouri University of Science and Technology Department of Chemistry research laboratories. The ^{1}H, ^{13}C, HSQC, and COSY NMR spectra were measured using a 400 MHz liquid NMR spectrometer with TMS as an internal standard and the spectra are shown in the Supporting Information. Bruker Top Spin version 3.6.1 was used for the analysis.

3.1.2. General Synthesis of 1−4. 4-Methoxycinnamaldehyde and diethyl (4-halobenzyl)phosphonate were mixed in a 1:1 molar ratio in a 50 mL round-bottomed flask and dissolved in 25 mL of THF. The

solution was cooled to 0 °C. NaH in 60% oil dispersion (1.6 times that of reactants) was added to the mixture, and the reaction was stirred at room temperature. After at least 12 h of stirring, THF was evaporated in a water bath at 80 °C. The remaining solution was cooled to room temperature and diluted with ice-cold water before vacuum filtration. The yellow filtrate was dried and then dissolved in chloroform. The crude product was filtered through filter paper into a breaker to remove any insoluble materials, and any remaining aqueous layer was removed via a separatory funnel liquid−liquid separation. The organic layer was concentrated in vacuo at 80 °C to remove all remaining solvent. The residue was removed from the flask to yield the products **1−4** as yellow powders.

3.1.2.1. 1-(4′-Fluorophenyl)-4-(4″-methoxyphenyl)buta-1,3-diene (1). 4-Methoxycinnamaldehyde (5.27 g, 3.25 mmol), diethyl (4-fluorobenzyl)phosphonate (0.69 mL, 3.25 mmol), and NaH in 60% oil dispersion (0.125 g, 5.20 mmol) were used. The reaction produced 0.46 g of **1** (55.8% yield). ^{1}H NMR (400 MHz, CDCl$_3$), δ (in ppm): 3.68 (s, 3H), 6.45 (t, 2H), 6.69 (q, 4H), 6.87 (t, 2H), 7.24 (q, 4H). ^{13}C NMR (400 MHz, CDCl$_3$), δ (in ppm): 55.3 (1C), 114.2 (2C), 115.7 (2C), 127.5 (1C), 130.1 (6C), 130.4 (1C), 132.7 (2C), 159.6 (1C), 161.9 (1C).

3.1.2.2. 1-(4′-Chlorophenyl)-4-(4″-methoxyphenyl)buta-1,3-diene (2). 4-Methoxycinnamaldehyde (1.00 g, 6.17 mmol) and diethyl (4-chlorobenzyl)phosphonate (1.36 mL, 6.17 mmol) were used. The reaction produced 1.37 g of **2** (81.8% yield). ^{1}H NMR (400 MHz, CDCl$_3$), δ (in ppm): 3.70 (s, 3H), 6.45 (d, 1H), 6.53 (d, 1H), 6.75 (q, 4H), 7.16 (d, 2H), 7.19 (d, 2H), 7.23 (d, 2H). ^{13}C NMR (400 MHz, CDCl$_3$), δ (in ppm): 55.4 (1C), 114.2 (2C), 127.3 (1C), 128.8 (4C), 130.1 (4C), 136.0 (4C), 159.4 (1C).

3.1.2.3. 1-(4′-Bromophenyl)-4-(4″-methoxyphenyl)buta-1,3-diene (3). 4-Methoxycinnamaldehyde (1.01 g, 6.20 mmol) and diethyl (4-bromobenzyl)phosphonate (1.39 mL, 6.20 mmol) were used. The reaction produced 1.23 g of **3** (63.2% yield). ^{1}H NMR (400 MHz, CDCl$_3$), δ (in ppm): 3.82 (s, 3H), 6.52 (d, 1H), 6.62 (d, 1H), 6.86 (q, 4H), 7.26 (d, 2H), 7.36 (d, 2H), 7.42 (d, 2H). ^{13}C NMR (400 MHz, CDCl$_3$), δ (in ppm): 55.3 (1C), 114.2 (2C), 122.8 (1C), 127.5 (1C), 128.6 (2C), 130.0 (4C), 130.9 (2C), 133.5 (2C), 134.2 (1C), 160.2 (1C).

3.1.2.4. 1-(4′-Iodophenyl)-4-(4″-methoxyphenyl)buta-1,3-diene (4). 4-Methoxycinnamaldehyde (1.78 g, 10.98 mmol) and diethyl (4-iodobenzyl)phosphonate (1.55 mL, 10.99 mmol) were used. The reaction produced 1.75 g of **4** (62.8% yield). ^{1}H NMR (400 MHz, CDCl$_3$), δ (in ppm): 1.13 (s, 3H), 2.96 (q, 2H), 3.90 (m, 6H), 6.93 (d, 2H), 7.51 (d, 2H). ^{13}C NMR (400 MHz, CDCl$_3$), δ (in ppm): 55.8 (1C), 93.5 (1C), 114.2 (2C), 127.7 (1C), 130.3 (4C), 133.2 (2C), 134.1 (1C), 134.6 (2C), 137.7 (2C), 159.0 (1C).

3.1.2.5. Diethyl (4-Iodobenzyl)phosphonate (15). 4-Iodobenzyl bromide (2.00 g, 6.75 mmol) and triethyl phosphite (1.76 mL, 10.17 mmol) were stirred together in a 50 mL round-bottom flask. A vacuum distillation apparatus was attached to the flask and any ethyl bromide formed during the reaction was collected. The reaction was heated under reduced pressure for 1 h at 130 °C. The dark purple solution remaining in the flask was concentrated in vacuo at 80 °C to afford product **15** as a dark, viscous oil (1.55 mL, 99.2% yield), and this product was used for the synthesis of **4**. ^{1}H NMR (400 MHz, CDCl$_3$): δ = 3.82 (s, 3H), 6.52 (d, 1H), 6.62 (d, 1H), 6.86 (q, 4H), 7.26 (d, 2H), 7.36 (d, 2H), 7.42 (d, 2H). ^{13}C NMR (400 MHz, CDCl$_3$), δ (in ppm): 16.3 (2C), 39.5 (1C), 62.2 (2C), 91.3 (1C), 130.6 (2C), 131.6 (1C), 137.5 (2C).

3.2. Crystallization. Crystals of the size 0.2−0.3 mm were grown from pure (MeO, Y)-BD samples using various solvents (acetone, chloroform, ethyl acetate/hexane mixture, ethanol, toluene) via slow evaporation technique. Chloroform and toluene resulted in X-ray quality crystals.

3.3. Computational Details. The crystal structure analyses were performed using Mercury[46] and CrystalExplorer[47] software. The bilayer packing diagrams and molecular stick models for description of intralayer, and interlayer interactions were generated in Mercury. The Hirshfeld surface analysis and the resulting 2D-fingerprint plots were generated using CrystalExplorer.

The potential energy surface analyses and property computations for (MeO, Y)-butadienes, (MeO, Y)-azines and p-nitroaniline (PNA) employed density functional theory (DFT).[48] Calculations were performed at the APFD/6-311G* level with Gaussian software.[49] The Austin−Frisch−Petersson functional with dispersion[50] (APFD) was combined with the polarized valence triple-ζ basis set 6-311G*.[51] No standard 6-311G* basis set is available for iodine and we employed the [10s,9p,5d] contraction of the (15s,12p,7d) basis set listed on the basis set exchange Web site.[52] All structure optimizations were followed by analytical computation of the vibrational frequencies to confirm that a stationary point had been reached, to determine the nature of the stationary structure (minimum or transition state), and to determine the molecular thermochemistry. Solvation Model Density (SMD)[42] method was employed to model bulk solvation. Molecular dipole moments μ_m and static first-order hyperpolarizabilities[53] β_o were computed for the free and the solvated molecules.

3.4. Crystal Structure Refinements. Single-crystal X-ray diffraction (SCXRD) data for **1**, **2**, (Pna2$_1$), **3**, and **4** were measured on a Bruker D8 Venture diffractometer equipped with a Photon 100 detector (**1**) or a Photon II detector (**2−4**) using Mo−Kα radiation from a microfocus source (Bruker AXS, Madison, WI). Data for **2** (Pbca) was measured on a Bruker X8 Prospector diffractometer equipped with an Apex II CCD area detector using Cu−Kα radiation from a microfocus source (Bruker-AXS). Crystals were cooled to their respective collection temperatures under streams of cold N$_2$ gas using Oxford Cryostream 700 or Cryostream 800 cryostats (Oxford Cryosystems, Oxford, U.K.). Hemispheres of data were collected for each sample using strategies of scans about the omega and phi axes. Unit cell determination, data collection, data reduction, absorption correction and scaling, and space group determination were performed using the Bruker Apex3 and Apex4 software suites.[54,55]

The crystal structures were solved by direct methods using SHELXS[56] and refined by full-matrix least-squares refinement using SHELXL.[57] Olex2 was used as an interface for model building and structure visualization.[58] PLATON was used for quantitative tests of crystallographic symmetry.[59] Full occupancy non-hydrogen atoms could be located from the difference map and refined anisotropically. In all refinements hydrogen atom positions and thermal parameters were constrained to ride on their carrier atoms.

4. CONCLUSIONS

The synthesis is described of a series of 1-(4′-halophenyl)-4-(4″-methoxyphenyl)buta-1,3-dienes with halogens F (**1**), Cl (**2**), Br (**3**), and I (**4**), and chromophores **1-4** were fully characterized. The single-crystal X-ray diffraction analyses established that **1-4** present a new class of highly dipole parallel-aligned organic materials for nonlinear optics (NLO). All molecules form PBAMs with perfect dipole parallel-alignment. As described, this conclusion was not reached in a straightforward manner because standard space group assignments indicated disordered structures in two cases. The correct crystal structure solutions were revealed only because of the results of measurements of bulk properties. Hence, our work exemplifies that bulk measurements on molecular materials are critical to fully understand interactions at the atomic level.

The PBAMs are held together by a new type of lateral arene−arene double T-contact. The double T-contacts feature a longitudinal offset which causes leaning angles of about 21°. The PBAMs are stacked with polarity enhancement in all cases. The 3D dipole parallel-alignment is perfect for fluoro compound **1**, that is, the chromophores in the successive PBAMs lean exactly in the same direction. In contrast, the PBAM orientation alternates in **2-4** and results in kink angles of about 138° and 66% of maximum possible polarity.

Because of the lateral offset of the two arenes within each 1,4-diphenylbutadiene, the formation of (felfe) double T-

contacts between neighboring chromophores is not necessarily expected especially because the lateral offset of the butadiene spacer would easily be accommodated by a normal π-stacking of both arenes in (fflff) contacts. However, the very occurrence of double T-contacts attests to their strength, and we explained how the lateral offset can be accommodated in butadiene pairs. Our crystal structure analyses clearly establish why the butadienes must adopt nonplanar structures in which the arenes remain parallel but are no longer coplanar. This discussion highlighted the origin of the helicity of the butadienes, and we described a method that relates the structural distortions with P- and M-helicity, respectively. The crystal structures of 1−4 all are true racemates.

The origin of kink angles in 2−4 is well understood as a direct consequence of directional MeO···Y halogen bonding across PBAMs. In sharp contrast, fluorine does not engage in MeO···F halogen bonding at all. Instead, the interlayer interactions in 1 involve F···H_{MeO} and O···H_o contacts which are corroborated by Hirshfeld analyses. In the absence of strong directional preferences of interlayer binding, the perfect polar stacking will always be preferred for electrostatic reasons.

The static first-order molecular hyperpolarizabilities β_o were computed for the free and solvated molecules, determined for the solution phase using the Lippert−Mataga Equation, and quantified in the solid state by powder SHG measurements. Analysis of the frontier orbitals shows that the electronic excitation of X−Ph−CR=E−E=CR−Ph−Y is associated with E → CR−Ar charge density shifts. This electronic reorganization upon excitation requires much less energy for the butadienes (CH → CR−Ar) than for the azines (N → CR−Ar) and results in much lower excitation energies for the former. It is this significant difference in the HOMO−LUMO gaps that provides a clear advantage to butadiene based NLO materials. The electronic excitation is greatly facilitated in condensed media because of the stabilization of the highly polar excited state ($\Delta\mu_{ex} > 6$ au or 15 D), and therefore, the β_o values computed and measured for the solvated chromophores greatly exceed the respective value of the free molecules (by factors between 2 to 5).

Among all the halogenated chromophores within a series, the fluoro compound always exhibits the lowest β_o value for the molecule. Yet, the fluorinated chromophore is the big winner in the powder SHG measurements because of the supramolecular structure. All chromophores 1−4 realize perfectly dipole parallel-aligned PBAMs, but only the fluoro chromophore 1 is capable of perfect polar PBAM stacking while the polar PBAM stacking in 2−4 is somewhat diminished because of the kink angles. This result emphasizes the great importance of the nature of the interlayer interaction for the overall solid-state property. The crystal structure of 1 presents only the third example of a perfectly dipole parallel-aligned material and the two previous examples (Me, PhO, F)-azine[20] and (Me, MeO−Ph, F)-azine[32] also are fluorinated chromophores.

ASSOCIATED CONTENT

ⓢ Supporting Information

The Supporting Information is available free of charge at https://pubs.acs.org/doi/10.1021/acs.chemmater.4c01744.

Hirshfeld surfaces and 2D fingerprint plots, solvent parameters, plots of $\Delta\nu_{ex}$ as a function of Δf, measured solvent dependency of absorption and emission maxima,

^1H and ^{13}C NMR spectra, COSY and HSQC NMR spectra, SS-FTIR spectra, and Cartesian coordinates of the optimized structures and thermochemical energies (PDF)

AUTHOR INFORMATION

Corresponding Author

Rainer Glaser − Department of Chemistry, Missouri University of Science and Technology, Rolla, Missouri 65409, United States; ⓞ orcid.org/0000-0003-3673-3858; Email: glaserr@mst.edu

Authors

Harmeet Bhoday − Department of Chemistry, Missouri University of Science and Technology, Rolla, Missouri 65409, United States

Justin Nulsen − Department of Chemistry, Missouri University of Science and Technology, Rolla, Missouri 65409, United States

Steven P. Kelley − Department of Chemistry, University of Missouri, Columbia, Missouri 65211, United States; ⓞ orcid.org/0000-0001-6755-4495

Complete contact information is available at:
https://pubs.acs.org/10.1021/acs.chemmater.4c01744

Notes

The authors declare no competing financial interest.

ACKNOWLEDGMENTS

REFERENCES

(1) Zheng, Y.; Cheng, P.; Qian, X.; Guan, J.; Shi, R.; Xin, M.; Xu, J.; Bu, X. Self-assembled organic nonlinear optical crystals based on pyridine derived fluorenone. *Mater. Chem. Front.* **2023**, 7, 698−704.

(2) Akiyoshi, R.; Hayami, S. Ferroelectric coordination metal complexes based on structural and electron dynamics. *Chem. Commun.* **2022**, 58, 8309−8321.

(3) Liu, X.; Yang, Z.; Wang, D.; Cao, H. Molecular Structures and Second-Order Nonlinear Optical Properties of Ionic Organic Crystal Materials. *Crystals* **2016**, 6 (12), No. 158.

(4) Tong, T.; Zhang, W.; Yang, Z.; Pan, S. Series of Crystals with Giant Optical Anisotropy: A Targeted Strategic Research. *Angew. Chem., Int. Ed.* **2021**, 60, 1332−1338.

(5) Kim, S. J.; Kang, B. J.; Puc, U.; Kim, W. T.; Jazbinsek, M.; Rotermund, F.; Kwon, O. P. Highly Nonlinear Optical Organic Crystals for Efficient Terahertz Wave Generation, Detection, and Applications. *Adv. Opt. Mater.* **2021**, 9, No. 2101019.

(6) Ghosh, T.; Mondal, M.; Vijayaraghavan, R. K. Minute torsional reorganization elicited a large visible-range fluorescence gain in terphenyl-derived crystals. *Mater. Chem. Front.* **2022**, 6, 297−305.

(7) Mencaroni, L.; Bonaccorso, C.; Botti, V.; Carlotti, B.; Consiglio, G.; Elisei, F.; Fortuna, C. G.; Spalletti, A.; Cesaretti, A. Nonlinear optical properties of a new panchromatic series of water-soluble bicationic push-pull fluorophores. *Dyes Pigm.* **2021**, 194, No. 109620.

(8) Horiuchi, S.; Tokura, Y. Organic ferroelectrics. *Nat. Mater.* **2008**, 7, 357−366.

(9) Steiger, D.; Ahlbrandt, C.; Glaser, R. Crystal Potential Formula for the Calculation of Crystal Lattice Sums. *J. Phys. Chem. B* **1998**, 102, 4257−4260.

(10) Chen, G. S.; Wilbur, J. K.; Barnes, C. L.; Glaser, R. Push-Pull Substitution versus Intrinsic or Packing Related N-N Gauche Preferences in Azines. Synthesis, Crystal Structures and Packing of

Asymmetrical Acetophenone Azines. *J. Chem. Soc., Perkin Trans. 2* **1995**, 2311−2317.

(11) Lewis, M.; Barnes, C. L.; Glaser, R. 4-Chloroacetophenone-(4-methoxyphenylethylidene) hydrazone. *Acta Crystallogr., Sect. C: Cryst. Struct. Commun.* **2000**, *56*, 393−396.

(12) Lewis, M.; Barnes, C. L.; Glaser, R. Near-Perfect Dipole Parallel-Alignment in the Highly Anisotropic Crystal Structure of 4-Iodoacetophenone-(4-methoxyphenylethylidene) Hydrazone. *J. Chem. Crystallogr.* **2000**, *30*, 489−496.

(13) Lewis, M.; Barnes, C. L.; Glaser, R. 4-Chloroacetophenone-4-Methoxyacetophenone Azine. *CSD Commun.* **2000**, No. 143276.

(14) Lewis, M.; Barnes, C. L.; Glaser, R. 4-Methoxyacetophenone-4-Iodoacetophenone Azine. *CSD Commun.* **2001**, No. 165429.

(15) Glaser, R.; Knotts, N.; Yu, P.; Li, L.; Chandrasekhar, M.; Martin, C.; Barnes, C. L. Perfect polar stacking of parallel beloamphiphile layers. Synthesis, structure and solid-state optical properties of the unsymmetrical acetophenone azine DCA. *Dalton Trans.* **2006**, 2891−2899.

(16) Glaser, R. Polar Order by Rational Design: Crystal Engineering with Parallel Beloamphiphile Monolayers. *Acc. Chem. Res.* **2007**, *40*, 9−17.

(17) Knotts, N.; Glaser, R.; Barnes, C. L.; Kelley, S. P. 4-Decyloxyacetophenone 4-Chloroacetophenone Azine. *CSD Commun.* **2020**, No. 2040898.

(18) Knotts, N.; Glaser, R.; Barnes, C. L.; Kelley, S. P. 4-Decyloxyacetophenone 4-Fluoroacetophenone Azine. *CSD Commun.* **2020**, No. 2040896.

(19) Knotts, N.; Glaser, R.; Barnes, C. L.; Kelley, S. P. 4-Decyloxyacetophenone 4-Bromoacetophenone Azine. *CSD Commun.* **2020**, No. 2040895.

(20) Bhoday, H.; Lewis, M.; Kelley, S. P.; Glaser, R. Perfect Polar Alignment of Parallel Beloamphiphile Monolayers: Synthesis, Characterization, and Crystal Architectures of Unsymmetrical Phenoxy-Substituted Acetophenone Azines. *ChemPlusChem* **2022**, *87*, No. e202200224.

(21) Lewis, M.; Bhoday, H.; Barnes, C. L.; Kelley, S. P.; Glaser, R. Para-Fluoroacetophenone para-Phenoxyacetophenone Azine. *CSD Commun.* **2023**, No. 2234129.

(22) Lewis, M.; Bhoday, H.; Barnes, C. L.; Kelley, S. P.; Glaser, R. Para-Chloroacetophenone para-Phenoxyacetophenone Azine. *CSD Commun.* **2023**, No. 2017223.

(23) Lewis, M.; Bhoday, H.; Barnes, C. L.; Kelley, S. P.; Glaser, R. Para-Bromoacetophenone para-Phenoxyacetophenone Azine. *CSD Commun.* **2023**, No. 2014691.

(24) Lewis, M.; Bhoday, H.; Barnes, C. L.; Kelley, S. P.; Glaser, R. Para-Bromoacetophenone para-Phenoxyacetophenone Azine. *CSD Commun.* **2023**, No. 2014692.

(25) Lewis, M.; Bhoday, H.; Barnes, C. L.; Kelley, S. P.; Glaser, R. Para-Iodoacetophenone para-Phenoxyacetophenone Azine. *CSD Commun.* **2023**, No. 2017221.

(26) Lewis, M.; Bhoday, H.; Barnes, C. L.; Kelley, S. P.; Glaser, R. Para-Iodoacetophenone para-Phenoxyacetophenone Azine. *CSD Commun.* **2023**, No. 2017222.

(27) Walz, L.; Paulus, H.; Haase, W. Crystal and molecular structures of four mesogenic 4′-alkoxy-4-cyanobiphenyls. *Z. Kristallogr.* **1987**, *180*, 97−121.

(28) Zyss, J.; Ledoux, I.; Bertault, M.; Toupet, E. Dimethylamino-cyanobiphenyl (DMACB): a new optimized molecular crystal for quadratic nonlinear optics in the visible. *Chem. Phys.* **1991**, *150*, 125−135.

(29) Jagarlapudi, A. R. P. S.; Allen, F. H.; Allen, F. H.; Hoy, V. J.; Howard, J. A. K.; Thaimattam, R.; Biradha, K.; Desiraju, G. R. Design of an SHG-active crystal, 4-iodo-4′-nitrobiphenyl: the role of supramolecular synthons. *Chem. Commun.* **1997**, 101−102.

(30) Glaser, R.; Knotts, N.; Wu, Z.; Barnes, C. L. Dipole Parallel-Alignment in the Crystal Structure of a Polar Biphenyl: 4′-Acetyl-4-Methoxybiphenyl (AMB). *Cryst. Growth Des.* **2006**, *6*, 235−240.

(31) Glaser, R.; Knotts, N.; Wu, Z.; Barnes, C. L. 4′-Acetyl-4-Methoxybiphenyl (AMB). *CSD Commun.* **2006**, No. 296213.

(32) Bhoday, H.; Knotts, N.; Glaser, R. Perfect Polar Alignment of Parallel Beloamphiphile Layers: Improved Structural Design Bias Realized in Ferroelectric Crystals of the Novel ″Methoxyphenyl Series of Acetophenone Azines. *Chem. - Eur. J.* **2024**, *30* (26), No. e202401197, DOI: 10.1002/chem.202401197.

(33) Yang, K.; Corretjer, N.; Gadban, S.; Kelley, S. P.; Glaser, R.; Kozak, M. M.; Hathaway, B. A. 1-(4-methoxyphenyl)-4-(4-fluoro-phenyl)-(1E,3E)-buta-1,3-diene. *CSD Commun.* **2023**, No. 2294067.

(34) Yang, K.; Corretjer, N.; Gadban, S.; Kelley, S. P.; Glaser, R.; Kozak, M. M.; Hathaway, B. A. 1-(4-methoxyphenyl)-4-(4-chlor-ophenyl)-(1E,3E)-buta-1,3-diene. *CSD Commun.* **2023**, No. 2310885.

(35) Bhoday, H.; Nulsen, J.; Kelley, S. P.; Glaser, R. (E,E)-1-(4-bromophenyl)-4-(4-methoxyphenyl)buta-1,3-diene. *CSD Commun.* **2022**, No. 2203168.

(36) Bhoday, H.; Nulsen, J.; Kelley, S. P.; Glaser, R. (E,E)-1-(4-iodophenyl)-4-(4-methoxyphenyl)buta-1,3-diene. *CSD Commun.* **2023**, No. 2310884.

(37) Glaser, R.; Dendi, L. R.; Knotts, N.; Barnes, C. L. Ab Initio and Crystal Structures of (E,E)-1,4-Diphenylbutadiene: A New Type of Arene-Arene Double T-Contact and an Interesting Inter-Layer Cooperation Involving Diastereoisomeric Contacts. *Cryst. Growth Des.* **2003**, *3*, 291−300.

(38) Glaser, R.; Dendi, L. R.; Knotts, N.; Barnes, C. L. (E,E)-1,4-Diphenylbutadiene. *CSD Commun.* **2003**, No. 214764.

(39) Kukkonen, E.; Lahtinen, E.; Myllyperkiö, P.; Haukka, M.; Konu, J. Nonlinear optical properties of diaromatic stilbene, butadiene and thiophene derivatives. *New J. Chem.* **2021**, *45*, 6640−6650.

(40) Luo, J.; Xue, Z. Q.; Liu, W. M.; Wu, J. L.; Yang, Z. Q. Koopmans' Theorem for Large Molecular Systems within Density Functional Theory. *J. Phys. Chem. A* **2006**, *110*, 12005−12009.

(41) Allin, S. B.; Leslie, T. M.; Lumpkin, R. S. Solvent Effects in Molecular Hyperpolarizability Calculations. *Chem. Mater.* **1996**, *8*, 428−432.

(42) Marenich, A. V.; Cramer, C. J.; Truhlar, D. G. Universal Solvation Model Based on Solute Electron Density and on a Continuum Model of the Solvent Defined by the Bulk Dielectric Constant and Atomic Surface Tensions. *J. Phys. Chem. B* **2009**, *113*, 6378−6396.

(43) Reish, M. E.; Kay, A. J.; Teshome, A.; Asselberghs, I.; Clays, K.; Gordon, K. C. Testing Computational Models of Hyperpolarizability in a Merocyanine Dye Using Spectroscopic and DFT Methods. *J. Phys. Chem. A* **2012**, *116*, 5453−5463.

(44) Kurtz, S. K.; Perry, T. T. A Powder Technique for the Evaluation of Nonlinear Optical Materials. *J. Appl. Phys.* **1968**, *39*, 3798−3813.

(45) Ok, K. M.; Chi, E. O.; Halasyamani, P. S. Bulk characterization methods for non-centrosymmetric materials: second-harmonic generation, piezoelectricity, pyroelectricity, and ferroelectricity. *Chem. Soc. Rev.* **2006**, *35*, 710−717.

(46) Macrae, C. F.; Sovago, I.; Cottrell, S. J.; Galek, P. T. A.; McCabe, P.; Pidcock, E.; Platings, M.; Shields, G. P.; Stevens, J. S.; Towler, M.; Wood, P. A. Mercury 4.0: from visualization to analysis, design and prediction. *J. Appl. Crystallogr.* **2020**, *53*, 226−235.

(47) Spackman, P. R.; Turner, M. J.; McKinnon, J. J.; Wolff, S. K.; Grimwood, D. J.; Jayatilaka, D.; Spackman, M. A. CrystalExplorer: a program for Hirshfeld surface analysis, visualization and quantitative analysis of molecular crystals. *J. Appl. Crystallogr.* **2021**, *54*, 1006−1011.

(48) Jones, R. O. Density functional theory: Its origins, rise to prominence, and future. *Rev. Mod. Phys.* **2015**, *87*, No. 897.

(49) Frisch, M. J.; Trucks, G. W.; Schlegel, H. B.; Scuseria, G. E.; Robb, M. A.; Cheeseman, J. R.; Scalmani, G.; Barone, V.; Petersson, G. A.; Nakatsuji, H.; Li, X.; Caricato, M.; Marenich, A. V.; Bloino, J.; Janesko, B. G.; Gomperts, R.; Mennucci, B.; Hratchian, H. P.; Ortiz, J. V.; Izmaylov, A. F.; Sonnenberg, J. L.; Williams-Young, D.; Ding, F.; Lipparini, F.; Egidi, F.; Goings, J.; Peng, B.; Petrone, A.; Henderson, T.; Ranasinghe, D.; Zakrzewski, V. G.; Gao, J.; Rega, N.; Zheng, G.; Liang, W.; Hada, M.; Ehara, M.; Toyota, K.; Fukuda, R.; Hasegawa, J.; Ishida, M.; Nakajima, T.; Honda, Y.; Kitao, O.; Nakai, H.; Vreven, T.;

Throssell, K.; J A Montgomery, J. E., Jr.; Peralta, F.; Ogliaro, M. J.; Bearpark, J. J.; Heyd, E. N.; Brothers, K. N.; Kudin, V. N.; Staroverov, T. A.; Keith, R.; Kobayashi, J.; Normand, K.; Raghavachari, A. P.; Rendell, J. C.; Burant, S. S.; Iyengar, J.; Tomasi, M.; Cossi, J. M.; Millam, M.; Klene, C.; Adamo, R.; Cammi, J. W.; Ochterski, R. L.; Martin, K.; Morokuma, O.; Farkas, J. B.; Foresman; Fox, D. J. *Gaussian 16*, Revision C.01; Gaussian, Inc.: Wallingford CT, 2016.

(50) Austin, A.; Petersson, G. A.; Frisch, M. J.; Dobek, F. J.; Scalmani, G.; Throssell, K. A Density Functional with Spherical Atom Dispersion Terms. *J. Chem. Theory Comput.* **2012**, *8*, 4989−5007.

(51) Basis set McLean, A. D.; Chandler, G. S. Contracted Gaussian-basis sets for molecular calculations. 1. 2nd row atoms, Z = 11−18. *J. Chem. Phys.* **1980**, *72*, 5639−5648.

(52) Pritchard, B. P.; Altarawy, D.; Didier, B.; Gibson, T. D.; Windus, T. L. New Basis Set Exchange: An Open, Up-to-Date Resource for the Molecular Sciences Community. *J. Chem. Inf. Model.* **2019**, *59*, 4814−4820.

(53) Paschoal, D.; Santos, H. F. D. Assessing the quantum mechanical level of theory for prediction of linear and nonlinear optical properties of push-pull organic molecules. *J. Mol. Model.* **2013**, *19*, 2079−2090.

(54) *Apex3, AXScale, and SAINT*, version 2017.3−0; Bruker AXS, Inc.: Madison, WI, 2017.

(55) *Apex4, AXScale, and SAINT*, version 2022.1; Bruker AXS, Inc.: Madison, WI, 2022.

(56) Sheldrick, G. M. *SHELXS*, v.2013−1, 2013.

(57) Sheldrick, G. M. Crystal structure refinement with *SHELXL*. *Acta Crystallogr., Sect. C: Cryst. Struct. Commun.* **2015**, *71*, 3−8.

(58) Dolomanov, O. V.; Bourhis, L. J.; Gildea, R. J.; Howard, J. A. K.; Puschmann, H. *OLEX2:* A complete structure solution, refinement, and analysis program. *J. Appl. Crystallogr.* **2009**, *42*, 339−341.

(59) Spek, A. L. *PLATON: A Multipurpose Crystallographic Tool*, v.140621, 2021.